Meteoritics & Planetary Science 40, Nr 6, 817–840 (2005)
Abstract available online at http://meteoritics.org

Earth Impact Effects Program: A Web-based computer program for calculating the regional environmental consequences of a meteoroid impact on Earth

Gareth S. COLLINS,[1*] H. Jay MELOSH,[2] and Robert A. MARCUS[2]

[1]Impacts and Astromaterials Research Centre, Department of Earth Science and Engineering, Imperial College London, South Kensington Campus, London, SW7 2AZ, UK
[2]Lunar and Planetary Laboratory, University of Arizona, 1629 East University Boulevard, Tucson, Arizona 85721–0092, USA
[*]Corresponding author. E-mail: g.collins@imperial.ac.uk

(Received 29 July 2004; revision accepted 14 April 2005)

Abstract–We have developed a Web-based program for quickly estimating the regional environmental consequences of a comet or asteroid impact on Earth (www.lpl.arizona.edu/impacteffects). This paper details the observations, assumptions and equations upon which the program is based. It describes our approach to quantifying the principal impact processes that might affect the people, buildings, and landscape in the vicinity of an impact event and discusses the uncertainty in our predictions. The program requires six inputs: impactor diameter, impactor density, impact velocity before atmospheric entry, impact angle, the distance from the impact at which the environmental effects are to be calculated, and the target type (sedimentary rock, crystalline rock, or a water layer above rock). The program includes novel algorithms for estimating the fate of the impactor during atmospheric traverse, the thermal radiation emitted by the impact-generated vapor plume (fireball), and the intensity of seismic shaking. The program also approximates various dimensions of the impact crater and ejecta deposit, as well as estimating the severity of the air blast in both crater-forming and airburst impacts. We illustrate the utility of our program by examining the predicted environmental consequences across the United States of hypothetical impact scenarios occurring in Los Angeles. We find that the most wide-reaching environmental consequence is seismic shaking: both ejecta deposit thickness and air-blast pressure decay much more rapidly with distance than with seismic ground motion. Close to the impact site the most devastating effect is from thermal radiation; however, the curvature of the Earth implies that distant localities are shielded from direct thermal radiation because the fireball is below the horizon.

INTRODUCTION

Asteroid and comet impacts have played a major role in the geological and biological history of the Earth. It is widely accepted that one such event, 65 million years ago, perturbed the global environment so catastrophically that a major biological extinction ensued (Alvarez 1980). As a result, both the scientific community and the general populace are increasingly interested in both the threat to civilization and the potential environmental consequences of impacts. Previous papers have examined, in detail, the natural hazard associated with the major environmental perturbations caused by impact events (Toon et al. 1994, 1997). To provide a quick and straightforward method for estimating the severity of several of these environmental effects, we have developed a free-of-charge, easy-to-use Web page maintained by the University of Arizona, which is located at: www.lpl.arizona.edu/impacteffects. Our program focuses on the consequences of an impact event for the regional environment; that is, from the impact location to a few thousand km away. The purpose of this paper is to present and justify the algorithm behind our program so that it may be applied more specifically to important terrestrial impact events and its reliability and limitations may be understood.

Before describing our program in detail, we will briefly review the impact process and the related environmental consequences. The impact of an extraterrestrial object on Earth begins when the impactor enters the tenuous upper atmosphere. At this moment, the impactor is traveling at a speed of between 11 and 72 km s^{-1} on a trajectory anywhere between normal incidence (90° to the Earth's surface) and a grazing impact, parallel to the Earth's surface. The most likely impact angle is 45° (Shoemaker 1962). The impactor's

traverse of the atmosphere may disrupt and decelerate the impactor significantly—a process that greatly affects the environmental consequences of the collision. Small impactors are disrupted entirely during their atmospheric traverse, depositing their kinetic energy well above the surface and forming no crater. Larger objects, however, retain sufficient momentum through the atmosphere to strike the Earth with enough energy to excavate a large crater and initiate several processes that affect the local, regional, and even global environment.

The formation of an impact crater is an extremely complicated and dynamic process (Melosh 1989). The abrupt deceleration of a comet or asteroid as it collides with the Earth transfers an immense amount of kinetic energy from the impacting body to the target. As a result, the target and impactor are rapidly compressed to very high pressures and heated to enormous temperatures. Between the compressed and uncompressed material, a shock wave is created that propagates away from the point of impact. In the wake of the expanding shock wave, the target is comprehensively fractured, shock-heated, shaken, and set in motion—leading to the excavation of a cavity many times larger than the impactor itself. This temporary cavity (often termed the transient crater; Dence et al. 1977) subsequently collapses under the influence of gravity to produce the final crater form. As the crater grows and collapses, large volumes of rock debris are ejected onto the surface of the Earth surrounding the crater. Close to the crater rim, this "ejecta deposit" forms a continuous blanket smothering the underlying terrain; further out, the ejecta lands as a scattered assortment of fine-grained dust and larger bombs that may themselves form small secondary craters.

In addition to cratering the surface of the earth, an impact event initiates several other processes that may have severe environmental consequences. During an impact, the kinetic energy of the impactor is ultimately converted into thermal energy (in the impactor and target), seismic energy, and kinetic energy of the target and atmosphere. The increase in thermal energy melts and vaporizes the entire impactor and some of the target rocks. The hot plume of impact-generated vapor that expands away from the impact site (referred to as the "fireball") radiates thermal energy that may ignite fires and scorch wildlife within sight of the fireball. As the impact-generated shock wave propagates through the target, it eventually decays into elastic waves that travel great distances and cause violent ground shaking several crater radii away. In addition, the atmosphere is disturbed in a similar manner to the target rocks; a shock wave propagates away from the impact site compressing the air to high pressures that can pulverize animals and demolish buildings, vehicles, and infrastructure, particularly where constructional quality is poor. Immediately behind the high-pressure front, violent winds ensue that may flatten forests and scatter debris.

All of these impact-related processes combine and interact in an extremely complicated way that requires detailed observation, laboratory experiments, or computer models to fully simulate and understand. However, with certain simplifying assumptions, we can derive reasonable estimates of their consequences for the terrestrial environment. In the following sections, we describe each of the steps that allow us to achieve this in the Earth Impact Effects Program. We discuss how our program estimates: 1) the impact energy and average time interval between impacts of the same energy, somewhere on Earth; 2) the consequences of atmospheric entry; 3) for crater forming events, the resulting crater size and volume of the melt produced; 4) the thermal radiation damage from the fireball; 5) the impact-induced seismic shaking; 6) the extent and nature of the ejecta deposit; and 7) the damage caused by the blast wave. To clearly identify our algorithm in the following discussion, all of the equations that we implement in the code are labeled with an asterisk (*).

To make the program accessible to the broadest range of users, it was written with as few input parameters as possible. The program requests six descriptors, which are illustrated schematically in Fig. 1: the diameter of the impactor L_0 (we use the term impactor to denote the asteroid, comet or other extraterrestrial object considered), the impactor density ρ_i, the impact velocity v_0, the angle that the trajectory of the impactor subtends with the surface of the Earth at the impact point θ, the target type, and the distance away from the impact at which the user wishes to calculate the environmental consequences r. Three target types are possible: sedimentary rock, for which we assign a target density of $\rho_t = 2500$ kg m^{-3}, crystalline rock ($\rho_t = 2750$ kg m^{-3}), or a marine target, for which the program requests a water-layer depth d_w and assigns a density of $\rho_w = 1000$ kg m^{-3} for the water and a target density of $\rho_t = 2700$ kg m^{-3} for the rock layer below. The program offers the user a variety of options for units; however, in this paper, the units for all variables are the SI units (mks) unless otherwise stated.

IMPACT ENERGY AND RECURRENCE INTERVAL

The most fundamental quantity in assessing the environmental consequences of the impact is the energy released during the impact, which is related to the kinetic energy of the impactor E before atmospheric entry begins. At normal solar system impact speeds, E is approximately given as one half times the impactor mass m_i times the square of the impactor velocity v_0, which can be rewritten in terms of the meteoroid's density ρ_i and diameter L_0, assuming that the meteoroid is approximately spherical:

$$E = \frac{1}{2} m_i v_0^2 = \frac{\pi}{12} \rho_i L_0^3 v_0^2 \quad (1^*)$$

In fact, the program uses the relativistic energy equation to accommodate the requests of several science fiction writers. The program does not limit the impact velocity to

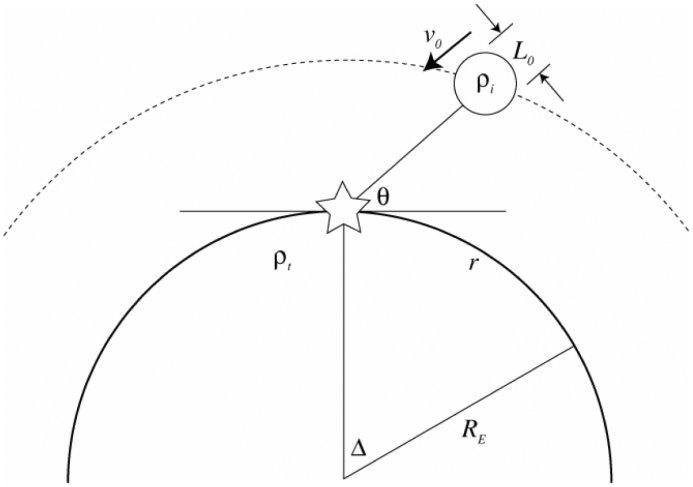

Fig. 1. Diagram illustrating the input parameters for the Earth Impact Effects Program: L_0 is the impactor diameter at the top of the atmosphere, v_0 is the velocity of the impactor at the top of the atmosphere, ρ_i is the impactor density, ρ_t is the target density, and θ is the angle subtended between the impactor's trajectory and the tangent plane to the surface of the Earth at the impact point. The distance r from the impact site at which the environmental consequences are determined is measured along the surface of the Earth; the epicentral angle Δ between the impact point and this distance r is given by $\Delta = r/R_E$, where R_E is the radius of the Earth.

72 km s^{-1}, the maximum possible for an impactor bound to the Sun; however, we have limited the maximum velocity to the speed of light, in response to attempts of a few users to insert supra-light velocities!

Natural objects that encounter the Earth are either asteroids or comets. Asteroids are made of rock (ρ_i ~2000–3000 kg m^3; Hilton 2002) or iron (ρ_i ~8000 kg m^3) and typically collide with the Earth's atmosphere at velocities of 12–20 km s^{-1} (Bottke et al. 1994). Detailed knowledge of the composition of comets is currently lacking; however, they are of much lower density (ρ_i ~500–1500 kg m^3) and are composed mainly of ice (Chapman and Brandt 2004). Typical velocities at which comets might encounter the Earth's atmosphere are in the range of 30–70 km s^{-1} (Marsden and Steel 1994). Thus, an asteroid or comet typically has 4–20 times the energy per unit mass of TNT at the moment atmospheric entry begins. Therefore, impact events have much in common with chemical and nuclear explosions, a fact that we will rely on later in our estimates of the environmental effects of an impact.

Observations of near-Earth objects made by several telescopic search programs show that the number of near-Earth asteroids with a diameter greater than L_{km} (in km) may be expressed approximately by the power law (Near-Earth Object Science Definition Team 2003):

$$N(>L) \approx 1148 L_{km}^{-2.354} \quad (2)$$

These data may also be represented in terms of the recurrence interval T_{RE} in years versus the impact energy E_{Mt} in megatons of TNT by assuming a probability of a single-object collision with Earth (~1.6×10^{-9} yr^{-1}; Near-Earth Object Science Definition Team 2003; their Fig. 2.3) and multiplying by the number of asteroids of a given potential impact energy that are estimated to be circling the sun with potentially hazardous, Earth-crossing orbits. We found that a simple power-law relationship adequately represents these data:

$$T_{RE} \approx 109 E_{Mt}^{0.78} \quad (3^*)$$

Thus, for a given set of user-input impact parameters (L_0, v_0, ρ_i, ρ_t, and θ), the program computes the kinetic energy (E_{Mt}, in megatons; 1 Mt = 4.18×10^{15} J) possessed by the impacting body when it hits the upper atmosphere and defines an average time interval between impacts of that energy, somewhere on the Earth. Furthermore, we estimate the recurrence interval T_{RL} for impacts of this same energy within a certain specified distance r of the impact. This is simply the product of the recurrence interval for the whole Earth and the fraction of the Earth's surface area that is within the distance r:

$$T_{RL} = \frac{T_{RE}}{2}(1 - \cos\Delta) \quad (4^*)$$

where Δ is the epicentral angle from the impact point to a range r (given in radians by: $\Delta = r/R_E$, where R_E is the radius of the Earth; Fig. 1).

Currently, the relative importance of comets to the Earth-crossing impactor flux is not well-constrained. The Near-Earth Object Science Definition Team (2003) suggests that comets comprise only about 1% of the estimated population of small NEOs; however, there is evidence to suggest that, at larger sizes, comets may comprise a significantly larger proportion of the impactor flux (Shoemaker et al. 1990). Of the asteroids that collide with the Earth's atmosphere, the current best estimate is that approximately 2–10% are iron asteroids (Bland and Artemieva 2003), based on NEO and main-belt asteroid spectroscopy (Bus et al. 2002; Binzel et al. 2003), meteorite composition, and the impactor types in large terrestrial craters.

ATMOSPHERIC ENTRY

Atmospheric entry of asteroids has been discussed in detail by many authors (Chyba et al. 1993; Ivanov et al. 1997; Krinov 1966; Melosh 1981; Passey and Melosh 1980; Svetsov et al. 1995; Korycansky et al. 2000, 2002; Korycansky and Zahnle 2003, 2004; Bland and Artemieva 2003) and is now understood to be a complex process, involving interaction of the atmosphere and fragmenting impactor in the Earth's gravitational field. For the purposes of a simple program of the type that we have created, many of the refinements now understood are too complex to be included. Therefore, we have opted to make a number of drastic simplifications that, we believe, will still give a good description of the basic events during atmospheric entry for most cases. Of course, for refined predictions, a full simulation using all of the known processes and properties must be undertaken. Atmospheric entry has no significant influence on the shape, energy, or

momentum of impactors with a mass that is much larger than the mass of the atmosphere displaced during penetration. For this reason, the program procedure described below is applied only for impactors less than 1 km in diameter.

For the purposes of the Earth Impact Effects Program, we assume that the trajectory of the impactor is a straight line from the top of the atmosphere to the surface, sloping at a constant angle to the horizon given by the user. Acceleration of the impactor by the Earth's gravity is ignored, as is deviation of the trajectory toward the vertical in the case that terminal velocity is reached, as it may be for small impactors. The curvature of the Earth is also ignored. The atmosphere is assumed to be purely exponential, with the density given by:

$$\rho(z) = \rho_0 e^{-z/H} \tag{5}$$

where z is the altitude above the surface, H is the scale height, taken to be 8 km on the average Earth, and ρ_0 is the surface atmospheric density, taken to be equal to 1 kg/m^3.

During the first portion of the impactor's flight, its speed is decreased by atmospheric drag, but the stresses are too small to cause fragmentation. Small meteoroids are often ablated to nothing during this phase, but in the current program implementation, we ignore ablation on the grounds that it seldom affects the larger impactors that reach the surface to cause craters. Thus, this program should not be used to estimate the entry process of small objects that may cause visible meteors or even drop small meteorites to the surface at terminal velocity.

While the body remains intact, the diameter of the incoming impactor is constant, equal to the diameter L_0 given by the user. The rate of change of the velocity v is given by the usual drag equation (corrected from Melosh 1989, chapter 11):

$$\frac{dv}{dt} = -\frac{3\rho z C_D}{4\rho_i L_0} v^2 \tag{6}$$

where C_D is the drag coefficient, taken to equal 2, and ρ_i is the impactor density (an input parameter). This equation can be greatly simplified by making the replacement $dt = -dz/v \sin\theta$ (justified by our assumption that the impactor travels in a straight line) and rearranging:

$$\frac{d \ln v}{dz} = \frac{3\rho(z) C_D}{4\rho_i L_0 \sin\theta} \tag{7}$$

Integration of this equation using the exponential density dependence gives the velocity of the impactor as a function of altitude:

$$v(z) = v_0 \exp\left\{-\frac{3\rho(z) C_D H}{4\rho_i L_0 \sin\theta}\right\} \tag{8*}$$

where θ is the entry angle, and v_0 is the impact velocity at the top of the atmosphere, given by the user.

As the impactor penetrates the atmosphere the atmospheric density increases and the stagnation pressure at the leading edge of the impactor, $P_s = \rho(z)\, v(z)^2$, rises. Eventually, this exceeds the strength of the impactor, and it begins to break up. Observed meteoroids often undergo several cascades of breakup, reflecting components of widely varying strengths. The entire subject of meteoroid strength is poorly understood, as measured crushing strengths of specimens collected on the ground are often a factor of 10 less than strengths inferred from observed breakup (Svetsov et al. 1995). Clearly, strong selection effects are at work. For the purposes of our program, we decided not to embroil the user in the ill-defined guesswork of estimating meteoroid crushing strength. Instead, we found a rough correlation between density and estimated strength for comets (about 15 Pa in tension from the tidal breakup of SL-9; Scotti and Melosh 1993), chondrites (Chyba et al. 1993), and iron or stone objects (Petrovic 2001). Based on four simplified estimates for comets, carbonaceous, stony, and iron meteorites, we established an empirical strength-density relation for use in the program. The yield strength Y_i of the impactor in Pa is thus computed from:

$$\log_{10} Y_i = 2.107 + 0.0624 \sqrt{\rho_i} \tag{9*}$$

where the impactor density ρ_i is in kg m^{-3}. Note that, even at zero density, this implies a non-zero strength of about 130 Pa. Thus, this empirical formula should not be applied too far out of the range of 1000 to 8000 kg m^{-3}, over which it was established.

Using this estimate of strength and comparing it to the stagnation pressure, we can compute an altitude of breakup z_* by solving the transcendental equation:

$$Y_i = \rho(z_*) v^2(z_*) \tag{10}$$

Rather than solving this equation in the program directly, an excellent analytic approximation to the solution was found and implemented:

$$z_* \approx -H\left[\ln\left(\frac{Y_i}{\rho_0 v_i^2}\right) + 1.308 - 0.314 I_f - 1.303\sqrt{1 - I_f}\right] \tag{11*}$$

where I_f is given by:

$$I_f = 4.07 \frac{C_D H Y_i}{\rho_i L_0 v_i^2 \sin\theta} \tag{12*}$$

In certain specific instances (i.e., small, strong impactors), the impactor may reach the surface intact; in this case, $I_f > 1$, and Equation 11 does not apply. The properly decremented velocity, calculated using Equation 8, is used to compute a crater size. (If this velocity happens to be less than the terminal velocity, then the maximum of the two is used instead.) The velocity at the top of the atmosphere and at the surface is reported.

Most often, the impactor begins to break up well above the surface; in this case, $I_f < 1$, and Equation 11 is used to

compute the breakup altitude z_*. After breakup, the fragments begin to disperse in a complex series of processes (Passey and Melosh 1980; Svetsov et al. 1995) that require detailed numerical treatment. However, a simple approximation to this cascade was found (Chyba et al. 1993; Melosh 1981), called the pancake model, that does a good job for Tunguska-class events. The basic idea of this model is that the impactor, once fractured, expands laterally under the differential pressure between the front and back surfaces. The front of the impactor is compressed at the stagnation pressure, and the rear is essentially in a vacuum with zero pressure. The sides squirt out at a rate determined by force balance in an inviscid fluid. This leads to a simple equation for the expansion of the impactor diameter L, now a function of time:

$$\frac{d^2L}{dt^2} = \frac{C_D P_s}{\rho_i L} = \frac{C_D \rho(z) v^2(z)}{\rho_i L} \tag{13}$$

The initial condition is that $L = L_0$ at $z = z_*$. If L does not increase too much over the scale height H, the time derivatives can be replaced with altitude derivatives (Chyba et al. 1993) and a nonlinear differential equation can be constructed that does not contain $v(z)$:

$$L\frac{d^2L}{dz^2} = \frac{C_D \rho(z)}{\rho_i \sin^2\theta} \tag{14}$$

Again, we construct an analytic approximation to the full solution of this equation, which is adequate for the purposes of the program:

$$L(z) = L_0\sqrt{1 + \left(\frac{2H}{l}\right)^2\left(\exp\left\{\frac{z_* - z}{2H}\right\} - 1\right)^2} \tag{15*}$$

where the dispersion length scale l is given by:

$$l = L_0 \sin\theta \sqrt{\frac{\rho_i}{C_D \rho(z_*)}} \tag{16*}$$

The velocity as a function of altitude is then given by inserting this expression for $L(z)$ into the drag equation and integrating downward from the breakup altitude z_*. Because of the rapid expansion of the pancake, the drag rises rapidly as well, and the velocity drops as a double exponential:

$$v(z) = v(z_*)\exp\left\{-\frac{3}{4}\frac{C_D \rho(z_*)}{\rho_i L_0^3 \sin\theta}\int_z^{z_*} e^{(z_* - z)/H} L^2(z)\,dz\right\} \tag{17*}$$

The crushed impactor spreads laterally until the ratio $L(z)/L_0$ reaches a prescribed limit, which we call the "pancake factor" f_p. In reality, this should be no larger than 2 to 4 (Ivanov et al. 1997), after which the fragments are sufficiently separated that they follow independent flight paths and may suffer one, or more, further pancake fragmentation events. However, Chyba et al (1993) obtained good agreement with Tunguska-class events using pancake factors as large as 5–10. In this work, we experimented with different factors and settled on a value of 7 to terminate the dispersion of the impactor. The altitude at which this dispersion is obtained is called the "airburst altitude" (z_b; see Fig. 2a); it is given by substituting $f_p = L(z)/L_0$ into Equation 15 and rearranging:

$$z_b = z_* - 2H \ln\left[1 + \frac{l}{2H}\sqrt{f_p^2 - 1}\right] \tag{18*}$$

If the airburst occurs above the surface (Fig. 2a), most of the energy is dissipated in the air. We report the airburst altitude z_b and the residual velocity of the swarm, which is computed using Equation 17. In this case, the integral in the exponent, evaluated from the airburst altitude to the disruption altitude, is given by:

$$\int_{z_{burst}}^{z_*} e^{(z_* - z)/H} L^2(z)\,dz = \frac{lL_0^2}{24}\alpha\left[8(3 + \alpha^2) + 3\alpha\frac{l}{H}(2 + \alpha^2)\right] \tag{19*}$$

with the definition $\alpha \equiv \sqrt{f_p^2 - 1}$. The surface impact velocity of the remnants from the airburst v_i is also reported as the maximum of the terminal velocity of a fragment half the diameter of the original impactor or the velocity of the swarm as a whole. The spreading velocity at airburst multiplied by the time to impact is added to the breadth of the swarm to estimate the dispersion of what will be a strewn field on the surface. The principal environmental consequence of such an event is a strong blast wave in the atmosphere (see below).

On the other hand, if the pancake does not spread to the limiting size before it reaches the ground ($z_b \le 0$ in Equation 19; Fig. 2b), the swarm velocity at the moment of impact is computed using Equation 17. In this case, the integral in the exponent, evaluated from the surface ($z = 0$) to the disruption altitude, is given by:

$$\int_0^{z_*} e^{(z_* - z)/H} L^2(z)\,dz = \frac{H^3 L_0^2}{3l^2}\left(34 + \left(\frac{l}{H}\right)^2 e^{z_*/H} + 6e^{2z_*/H} - 16e^{3z_*/2H} - 3\left(\frac{l}{H}\right)^2 - 2\right) \tag{20}$$

The dispersion of the swarm at impact is compared to the estimated transient crater size (see below) and, if it is comparable or larger, then the formation of a crater field is reported, similar to that actually observed at Henbury, Australia. Otherwise, we assume the impact to be a crater-

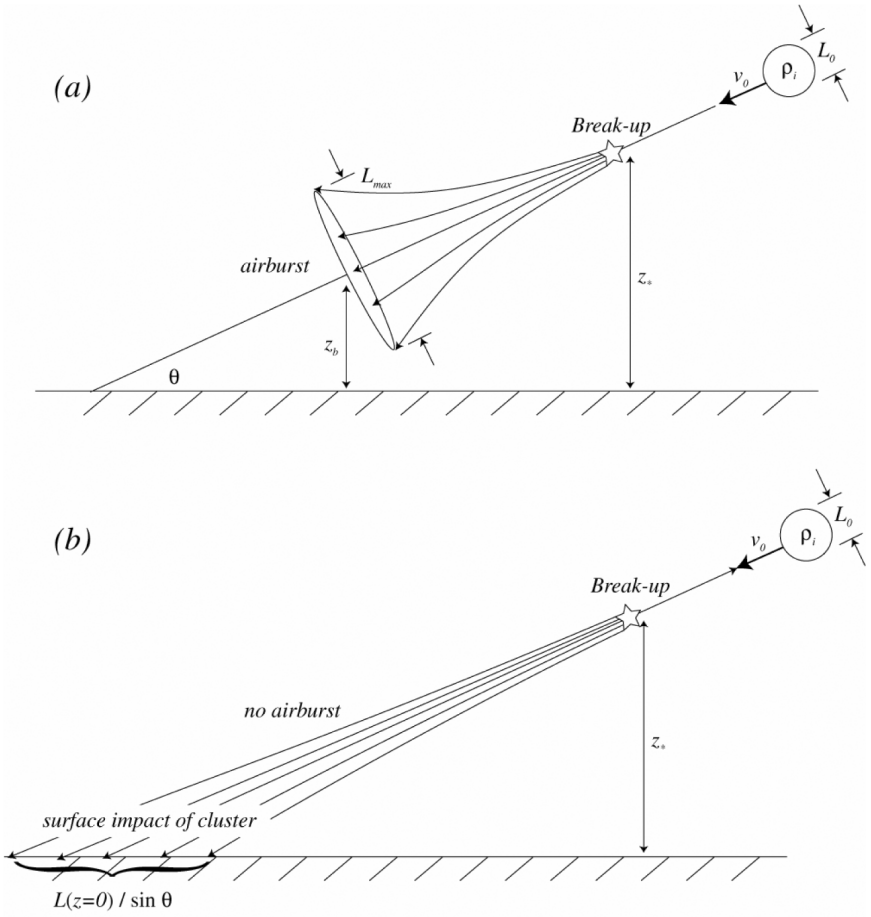

Fig. 2. Schematic illustration of two atmospheric entry scenarios considered in the Earth Impact Effects Program: a) the impactor (initial diameter L_0) begins to break up at an altitude z_*; from this point the impactor spreads perpendicular to the trajectory due to the different pressures on the front and back face. We define the airburst altitude z_b to be the height above the surface at which the impactor diameter $L(z) = 7L_0$. All the impact energy is assumed to be deposited at this altitude; no crater is formed, but the effects of the blast wave are estimated; b) the impactor breaks up but the critical impactor diameter is not reached before the fragmented impactor strikes the surface ($z_* > 0$; $z_b < 0$). The cluster of fragments impacts the target surface with a velocity v_i, forming a single crater or crater field depending on the lateral spread of the cluster, $L(z = 0)/\sin\theta$.

forming event and use the velocity at the surface to compute a crater size. In either case, the environmental consequences of these events are calculated based on an impact energy equal to the total kinetic energy of the swarm at the moment it strikes the surface.

Although simple, we have found the prescription above to give a fairly reasonable account of atmospheric entry over a wide range of impactor sizes and compositions. As mentioned above, a much more complex treatment must be made on a case-by-case basis if more exact results are needed. In particular, our program is not capable of providing a mass- or velocity-distribution for fragmented impactors and, therefore, cannot be used to model production of terrestrial crater fields where the size of the largest crater is related to the largest surviving fragment.

CRATER DIMENSIONS AND MELT PRODUCTION

Determining the size of the final crater from a given impactor size, density, velocity, and angle of incidence is not a trivial task. The central difficulty in deriving an accurate estimate of the final crater diameter is that no observational or experimental data exist for impact craters larger than a few tens of meters in diameter. Perhaps the best approach is to use sophisticated numerical models capable of simulating the propagation of shock waves, the excavation of the transient crater, and its subsequent collapse; however, this method is beyond the scope of our simple program. Instead, we use a set of scaling laws that extrapolate the results of small-scale experimental data to scales of interest or extend observations of cratering on other planets to the Earth. The first scaling law we apply is based on the work of Holsapple and Schmidt (1982), Schmidt and Housen (1987), and Gault (1974) and combines a wide range of experimental cratering data (for example, small-scale hypervelocity experiments and nuclear explosion experiments). The equation relates the density of the target ρ_t and impactor ρ_i (in kg m^{-3}), the impactor diameter after atmospheric entry L (in m), the impact velocity at the surface v_i (in m s^{-1}), the angle of impact θ (measured to the horizontal), and the Earth's surface gravity g_E (in m s^{-2}),

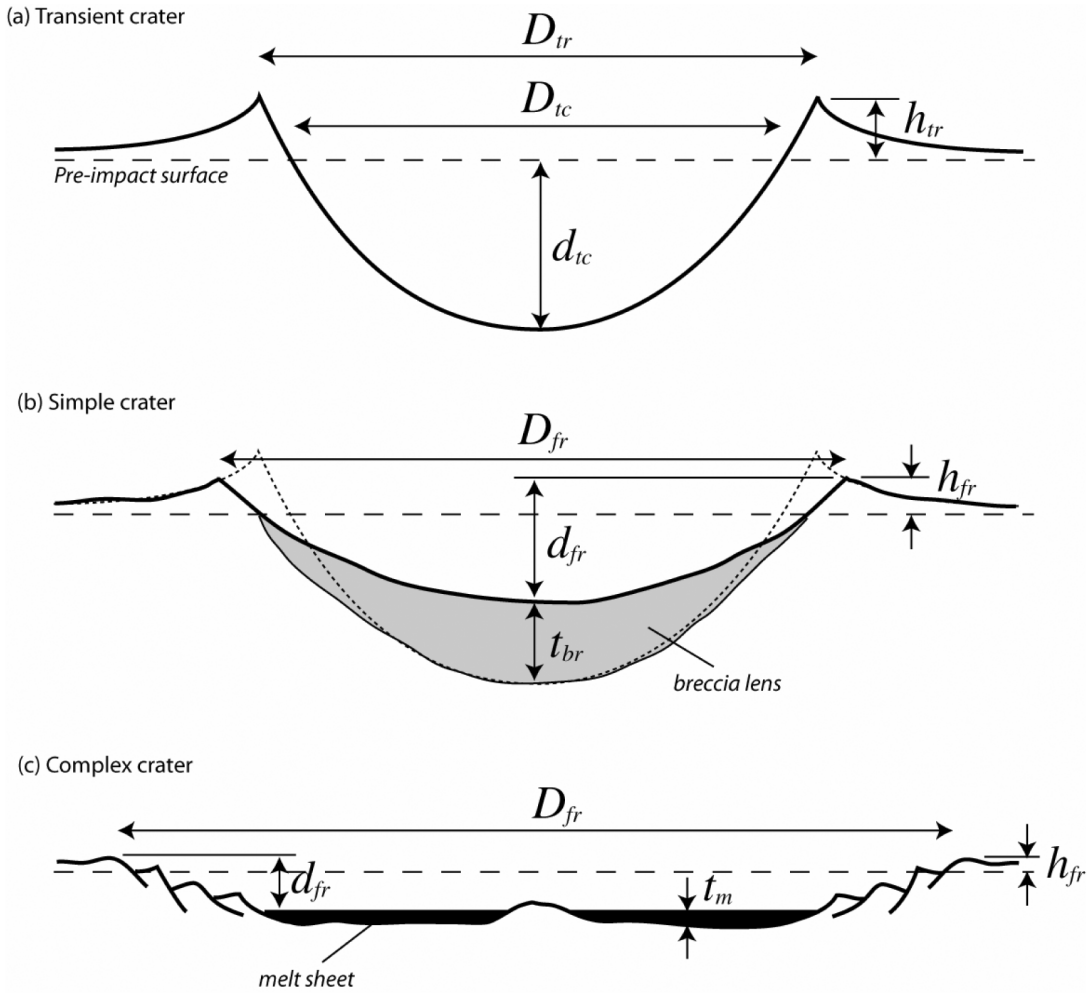

Fig. 3. Symbols used in the text to denote the various dimensions of an impact crater. a) Transient crater dimensions: D_{tc} is the transient crater diameter measured at the pre-impact surface; D_{tr} is the diameter of the transient crater measured from rim crest to rim crest; h_{tr} is the rim height of the transient crater measured from the pre-impact surface; d_{tc} is the depth of the transient crater measured from the pre-impact surface (we assume that $D_{tc} = 2\sqrt{2}\ d_{tc}$); b) simple crater dimensions (the transient crater outline is shown by the dotted line): D_{fr} is the rim-to-rim diameter; h_{fr} is the rim height above the pre-impact surface; t_{br} is the breccia lens thickness; d_{fr} is the crater depth measured from the crater floor (above the breccia lens) to the rim crest. We assume that the base of the breccia lens coincides with the floor of the transient crater at a depth of d_{tc} below the pre-impact surface; therefore, $d_{fr} = d_{tc} + h_{fr} - t_{br}$; c) complex crater dimensions: D_{fr} is the rim-to-rim diameter; h_{fr} is the rim height above the pre-impact surface; t_m is the melt sheet thickness; d_{fr} is the crater depth measured from the crater floor (above the melt sheet) to the rim crest.

to the diameter of the transient crater D_{tc} (in m) as measured at the pre-impact target surface (Fig. 3a):

$$D_{tc} = 1.161\left(\frac{\rho_i}{\rho_t}\right)^{1/3} L^{0.78} v_i^{0.44} g_E^{-0.22} \sin^{1/3}\theta \qquad (21^*)$$

This equation applies for impacts into solid rock targets where gravity is the predominant arresting influence in crater growth, which is the case for all terrestrial impacts larger than a couple of hundred meters in diameter. For impacts into water, the constant 1.161 must be replaced by 1.365 (Schmidt and Housen 1987). In reality, these constants are not known to three decimal places; the values quoted serve as a best estimate within a range of 0.8 to 1.5.

The transient crater is only an intermediate step in the development of the final crater (Fig. 3). To estimate the final crater diameter, we must consider the effect of the transient crater's collapse using another scaling law. For craters smaller than ~3.2 km in diameter on Earth (classified by Dence [1965] as "simple" based on their intuitive morphology), the collapse process is well-understood: highly brecciated and molten rocks that were originally pushed out of the opening crater slide back down the steep transient cavity walls forming a melt-and-breccia lens at the base of the crater (Grieve et al. 1977; Fig. 3a). To derive an estimate of the final crater diameter for simple craters, we applied an analytical model for the collapse of simple craters originally developed by Grieve and Garvin (1984) to two terrestrial craters for which good observational data on breccia-lens volume and final crater dimensions exist. In matching the observational data to model predictions we found that an excellent first order approximation is that the final rim-to-rim diameter D_{fr} for a simple crater is given approximately by:

$$D_{fr} \approx 1.25 D_{tc} \quad (22^*)$$

if the unbulked breccia lens volume V_{br} (i.e., the observed volume of the breccia lens multiplied by a 90–95% bulking correction factor; Grieve and Garvin 1984) is assumed to be related to the final crater diameter by:

$$V_{br} \approx 0.032 D_{fr}^3 \quad (23^*)$$

This approximate relationship is based on estimates of unbulked breccia-lens volumes at Meteor Crater and Brent Crater (Grieve and Garvin 1984).

The model may also be used to estimate the thickness of the breccia lens, the depth to the base of the breccia lens, and the final depth of the crater. Assuming that the top surface of the breccia lens is parabolic and that the brecciation process increases the bulk volume of this material by 10%, the thickness of the breccia lens t_{br} is given approximately by:

$$t_{br} = 2.8 V_{br} \left(\frac{d_{tc} + h_{fr}}{d_{tc} D_{fr}^2} \right) \quad (24^*)$$

where d_{tc} is the transient crater depth (below the original ground plane), and h_{fr} is the rim height (above the original ground plane) of the final crater (see the section below on ejecta deposits). The depth to the base of the breccia lens is taken to be the same as the transient crater depth d_{tc}, which we assume is given by:

$$d_{tc} = D_{tc} / (2\sqrt{2}) \quad (25^*)$$

based on observations by Dence et al. (1977). The depth of the final crater from the rim to the crater floor d_{fr} is then simply (see Fig. 3b):

$$d_{fr} = d_{tc} + h_{fr} - t_{br} \quad (26^*)$$

For craters larger than 3.2 km on Earth (termed complex because of their unintuitive morphology after Dence [1965]), the collapse process is less well-understood and involves the complicated competition between gravitational forces tending to close the transient crater and the strength properties of the post-impact target rocks. Several scaling laws exist for estimating the rim-to-rim diameter of a complex crater from the transient crater diameter, or vice versa, based on reconstruction of the transient craters of lunar complex craters (see, for example, Croft 1985; McKinnon and Schenk 1985; Holsapple 1993). We use the functional form:

$$D_{fr} = 1.17 \frac{D_{tc}^{1.13}}{D_c^{0.13}} \quad (27^*)$$

established by McKinnon and Schenk (1985), which lies intermediate between the estimates of Croft (1985) and Holsapple (1993). In this equation, D_c is the diameter at which the transition from simple to complex crater occurs (taken to be 3.2 km on Earth); both D_{tc} and D_{fr} are in km (See Fig. 3b). If the transient crater diameter is greater than 2.56 km, we apply Equation 27 to determine the final crater diameter and report that a "complex" crater is formed; otherwise, we apply Equation 22 and report that a "simple" crater is formed. It is worth emphasizing that the final crater diameter that the program reports is the diameter of the fresh crater measured from rim crest to rim crest (see Figs. 3b and 3c). The topographic rim is likely to be strongly affected by post-impact erosion. Furthermore, multiple concentric zones of structural deformation are often observable at terrestrial impact structures—a fact that has led to uncertainty in the relationship between the structural (apparent) and topographic (rim-to-rim) crater diameter (Turtle et al. 2005). Therefore, the results of the scaling arguments above should be compared with caution to apparent diameters of known terrestrial impact structures.

To estimate the average depth d_{fr} (in km) from the rim to floor of a complex crater of rim-to-rim diameter D_{fr} (in km), we use the depth-to-diameter relationship of Herrick et al. (1997) for venusian craters:

$$d_{fr} = 0.4 D_{fr}^{0.3} \quad (28^*)$$

The similarity in surface gravity between Earth and Venus as well as the large number of fresh complex craters on Venus makes this relationship more reliable than that based on the limited and erosion-affected data for terrestrial complex craters (Pike 1980; Grieve and Therriault 2004).

We also estimate the volume of melt produced during the impact event, based on the results of numerical modeling of the early phase of the impact event (O'Keefe and Ahrens 1982b; Pierazzo et al. 1997; Pierazzo and Melosh 2000) and geological observation at terrestrial craters (Grieve and Cintala 1992). Provided that: 1) the impact velocity is in excess of ~12 km s^{-1} (the threshold velocity for significant target melting, O'Keefe and Ahrens 1982b); 2) the density of the impactor and target are comparable; and 3) all impacts are vertical, these data are well-fit by the simple expression:

$$V_m = 0.25 \frac{v_i^2}{\varepsilon_m} V_i \quad (29)$$

where V_m is the volume of melt produced, V_i is the volume of the impactor, and ε_m is the specific energy of the Rankine-Hugoniot state from which the isentropic release ends at the 1 bar point on the liquidus. To avoid requiring further input parameters in our program, we use $\varepsilon_m = 5.2$ MJ/kg for granite (see Pierazzo et al. 1997), which we take as representative of upper-crustal rocks, and assume an impactor and target density of 2700 kg m^{-3}. This allows us to rewrite Equation 29, giving the impact melt volume V_m (in m^3) in terms of just the impact energy E (in J): $V_m = 8.9 \times 10^{-12} E$.

To account for the effect of impact angle on impact melt

production, we assume, based on numerical modeling work (Pierazzo and Melosh 2000; Ivanov and Artemieva 2002), that the volume of impact melt is roughly proportional to the volume of the transient crater. In our program, the diameter and depth of the transient crater are proportional to $\sin^{1/3}\theta$ (Equations 21 and 25); hence, the volume of the transient crater is proportional to $\sin\theta$. The equation used in our program to compute the impact melt volume is, therefore:

$$V_m = 8.9 \times 10^{-12}\, E \sin\theta \qquad (30^*)$$

This expression works well for all geologic materials except ice. In this case, V_m is about ten times larger than for rock (Pierazzo et al. 1997). Equation 30 neglects the effect of geothermal gradient on melt production. For very large impacts, which affect rocks deep in the Earth where ambient temperatures are much closer to the melting point, this expression will underestimate the volume of melt produced. Equation 30 agrees well with model predictions (Pierazzo and Melosh 2000) of impact melt volume versus impact angle for impact angles greater than ~15° to the horizontal; for impact angles of ~15° or less, Equation 30 probably overestimates the volume of impact melt produced by a factor of ~2.

In simple craters, the melt is well-mixed within the breccia lens on the floor of the crater; in larger complex craters, however, the melt forms a coherent sheet, which usually has an approximately uniform thickness across the crater floor (Grieve et al. 1977). Here we assume that the crater floor diameter is similar to the transient crater diameter (Croft 1985). Thus, we estimate the average thickness of this sheet t_m as the ratio of the melt volume to the area of a circle equal in diameter to the transient crater:

$$t_m = 4V_m/\pi D_{tc}^2 \qquad (31^*)$$

In extremely large terrestrial impact events (D_{tc} >1500 km), the volume of melt produced, as predicted by Equation 30, is larger than the volume of the crater. In this case, we anticipate that the transient crater would collapse to a hydrostatic, almost-featureless surface and, therefore, our program does not quote a final crater diameter. Instead of a topographically observable crater, the program postulates that a large circular melt province would be formed. We note, however, that no such feature has been unequivocally identified on Earth. Our program also compares the volume of impact-generated melt to the volume of the Earth and reports the fraction of the planet that is melted in truly gigantic impacts.

THERMAL RADIATION

As alluded to above, the compression of the target and impactor during the initial stages of an impact event drastically raises the temperature and pressure of a small region proximal to the impact site. For impacts at a velocity greater than ~12 km s^{-1}, the shock pressures are high enough to melt the entire impactor and some target material; vaporization also occurs for impacts at velocities greater than ~15 km s^{-1}. Any vapor produced is initially at very high pressure (>100 GPa) and temperature (>10,000 K) and, thus, begins to rapidly inflate; the expanding hot vapor plume is termed the "fireball." The high temperatures imply that thermal radiation is an important part of the energy balance of the expanding plume. Initially, the fireball is so hot that the air is ionized and its radiation absorption properties are substantially increased. As a result, the fireball is initially opaque to the emitted radiation, which remains bottled up within the ball of plasma. The actual process is much more complex than the simple description here and we refer the interested reader to Glasstone and Dolan (1977) for a more complete exposition. With continued expansion, the fireball cools; as the temperature approaches a critical temperature, known as the transparency temperature T_* (Zel'dovich and Raizer 1966, p. 607), the opacity rapidly diminishes and the thermal radiation escapes, bathing the Earth's surface in heat from the fireball. The thermal radiation lasts for a few seconds to a few minutes; the radiation intensity decays as the expanding fireball rapidly cools to the point where radiation ceases. For Earth's atmosphere, the transparency temperature is ~2000–3000 K (Nemtchinov et al. 1998); hence, the thermal radiation is primarily in the visible and infrared wavelengths—the fireball appears as a "second sun" in the sky. The transparency temperature of silicate vapor is about 6000 K (Melosh et al. 1993), so that the limiting factor for terrestrial impacts is the transparency temperature of air surrounding the silicate vapor fireball.

Provided that the impact velocity is in excess of 15 km s^{-1}, we estimate the fireball radius R_{f*} at the moment the transparency temperature is achieved, which we consider to be the time of maximum radiation. Numerical simulations of vapor plume expansion (Melosh et al. 1993; Nemtchinov et al. 1998) predict that the fireball radius at the time of maximum radiation is 10–15 times the impactor diameter. We use a value of 13 and assume "yield scaling" applies to derive a relationship between impact energy E in joules and the fireball radius in meters:

$$R_{f*} = 0.002E^{1/3} \qquad (32^*)$$

Yield scaling is the empirically derived concept that certain length and time scales measured for two different explosions (or impacts) are approximately identical if divided by the cube root of the yield (or impact) energy. Yield scaling can be justified theoretically, provided that gravity and rate-dependent processes do not strongly influence the measured parameters (Melosh 1989, p. 115). The constant in Equation 32 was found by dividing the fireball radius (given by $R_{f*} = 13L_0$) by the cube root of the impact energy (given by Equation 1), for a typical impactor density (2700 kg m^{-3}) and terrestrial impact velocity (20 km s^{-1}).

The time at which thermal radiation is at a maximum T_t is estimated by assuming that the initial expansion of the fireball occurs at approximately the same velocity as the impact:

$$T_t = \frac{R_{f*}}{v_i} \quad (33*)$$

To calculate the environmental effects of the thermal radiation from the fireball, we consider the heating at a location a distance r from the impact site. The total amount of thermal energy emitted as thermal radiation is some small fraction η (known as the "luminous efficiency") of the impact energy E. The luminous efficiency for hypervelocity impacts is not presently well-constrained. Numerical modeling results (Nemtchinov et al. 1998) suggest that η scales as some power law of impact velocity. The limited experimental, observational, and numerical results that exist indicate that for typical asteroidal impacts with Earth, η is in the range of 10^{-4}–10^{-2} (Ortiz et al. 2000); for a first-order estimate we assume $\eta = 3 \times 10^{-3}$ and ignore the poorly-constrained velocity dependence.

The thermal exposure Φ quantifies the amount of heating per unit area at our specified location. Φ is given by the total amount of thermal energy radiated ηE divided by the area over which this energy is spread (the surface area of a hemisphere of radius r, $2\pi r^2$):

$$\Phi = \frac{\eta E}{2\pi r^2} \quad (34*)$$

The total thermal energy per unit area Φ that heats our location of interest arrives over a finite time period between the moment the fireball surface cools to the transparency temperature and is unveiled to the moment when the fireball has expanded and cooled to the point where radiation ceases. We define this time period as the "duration of irradiation" τ_t. Without computing the hydrodynamic expansion of the vapor plume this duration may be estimated simply by dividing the total energy radiated per unit area (total thermal energy emitted per unit area of the fireball) by the radiant energy flux, given by σT_*^4, where $\sigma = 5.67 \times 10^{-8}$ W m^{-2} K^{-4} is the Stefan-Bolzmann constant. In our program, we use $T_* = 3000$ K. Then, the duration of irradiation is:

$$\tau_t = \frac{\eta E}{2\pi R_{f*}^2 \sigma T_*^4} \quad (35*)$$

For situations where the specified distance away from the impact point is so far that the curvature of the Earth implies that part of the fireball is below the horizon, we modify the thermal exposure Φ by multiplying by the ratio f of the area of the fireball above the horizon to the total area. This is given by:

$$f = \frac{2}{\pi}\left(\delta - \frac{h}{R_{f*}}\sin\delta\right) \quad (36*)$$

In this equation, h is the maximum height of the fireball below the horizon as viewed from the point of interest, given by:

$$h = (1 - \cos\Delta)R_E \quad (37*)$$

where Δ is the epicentral angle between the impact point and the point of interest, and R_E is the radius of the Earth. If $h \geq R_{f*}$, then the fireball is entirely below the horizon; in this case, no direct thermal radiation will reach our specified location. The angle δ in Equation 36 is half the angle of the segment of the fireball visible above the horizon, given by $\delta = \cos^{-1} h/R_{f*}$. We presently ignore atmospheric refraction and extinction for rays close to the horizon (this effect is important only over a small range interval).

Whether a particular material catches fire as a result of the fireball heating depends not only on the corrected thermal exposure $f\Phi$ but also on the duration of irradiation. The thermal exposure $\Phi_{ignition}$ (J m^{-2}) required to ignite a material, that is, to heat the surface to a particular ignition temperature $T_{ignition}$, is given approximately by:

$$\Phi_{ignition} \approx T_{ignition}\rho c_p\sqrt{\kappa\tau_t} \quad (38)$$

where ρ is the density, c_p is the heat capacity, and κ is the thermal diffusivity of the material being heated. This expression equates the total radiant energy received per unit area, on the left, to the heat contained in a slab of unit area perpendicular to the fireball direction, on the right. The thickness of the slab is estimated from the depth, $\sqrt{\kappa\tau_t}$, penetrated by the thermal wave during the irradiation time τ_t. Analysis of Equation 35 shows that τ_t is proportional to the thermal exposure divided by the fireball radius squared. Hence, the duration of irradiation is proportional to $E^{1/3}$, and the thermal exposure required to ignite a given material is proportional to $E^{1/6}$. This simple relationship is supported by empirical data for the ignition of various materials by thermal radiation from nuclear explosion experiments over a range of three orders of magnitude in explosive yield energy (Glasstone and Dolan 1977, p. 287–289). Thus, although a more energetic impact event, or explosion, implies a greater total amount of thermal radiation, this heat arrives over a longer period of time, and hence, there is more time for heat to be diluted by conduction through the material. This results in a greater thermal exposure being required to ignite the same material during a more energetic impact event.

To account for the impact-energy dependence of the thermal exposure required to ignite a material (or cause skin damage), we use a simple scaling law. We estimate the thermal exposure required to ignite several different materials, or burn skin, during an impact of a given energy by multiplying the thermal exposure required to ignite the material during a 1 Mt event (see Table 1; data from Glasstone and Dolan 1977, p. 287–289) by the impact energy (in MT) to the one-sixth power:

$$\Phi_{ignition}(E) = \Phi_{ignition}(1\text{ Mt})E_{Mt}^{1/6} \quad (39*)$$

To assess the extent of thermal radiation damage at our location of interest, we compute the thermal radiation

Table 1. Ignition factors for various materials.[a]

Material	Thermal exposure required to ignite material during a 1 Mt explosion ($\Phi_{ignition}$(1 Mt), MJ m^{-2})
Clothing	1.0
Plywood	0.67
Grass	0.38
Newspaper	0.33
Deciduous trees	0.25
Third degree burns	0.42
Second degree burns	0.25
First degree burns	0.13

[a]Data extracted from Glasstone and Dolan (1977).

Table 2. Seismic magnitude/Modified Mercalli Intensity.[a]

Richter magnitude	Modified Mercalli Intensity
0–1	–
1–2	I
2–3	I–II
3–4	III–IV
4–5	IV–V
5–6	VI–VII
6–7	VII–VIII
7–8	IX–X
8–9	X–XI
9+	XII

[a]Based on data from Richter (1958).

exposure $f\Phi$ and compare this with $\Phi_{ignition}$ (calculated using Equation 39) for each type of damage in Table 1. For thermal exposures in excess of these ignition exposures, we report that the material ignites or burns.

Our simple thermal radiation model neglects the effect of both atmospheric conditions (cloud, fog, etc.) and the variation in atmospheric absorption with altitude above the horizon. Experience from nuclear weapons testing (Glasstone and Dolan 1977, p. 279) suggests that, in low visibility conditions, the reduction in direct (transmitted) radiation is compensated for, in large part, by indirect scattered radiation for distances less than about half the visibility range. This observation led Glasstone and Dolan (1977) to conclude that "as a rough approximation, the amount of thermal energy received at a given distance from a nuclear explosion may be assumed to be independent of the visibility." Hence, although the above estimate should be considered an upper estimate on the severity of thermal heating, it is probably quite reliable, particularly within half the range of visibility.

SEISMIC EFFECTS

The shock wave generated by the impact expands and weakens as it propagates through the target. Eventually, all that remains are elastic (seismic) waves that travel through the ground and along the surface in the same way as those excited by earthquakes, although the structure of the seismic waves induced by these distinct sources is likely to be considerably different.

To calculate the seismic magnitude of an impact event, we assume that the "seismic efficiency" (the fraction of the kinetic energy of the impact that ends up as seismic wave energy) is one part in ten thousand (1×10^{-4}). This value is the most commonly accepted figure based on experimental data (Schultz and Gault 1975), with a range between 10^{-5}–10^{-3}. Using the classic Gutenberg-Richter magnitude energy relation, the seismic magnitude M is then:

$$M = 0.67\log_{10} E - 5.87 \qquad (40^*)$$

where E is the kinetic energy of the impactor in Joules (Melosh 1989, p. 67).

To estimate the extent of devastation at a given distance from a seismic event of this magnitude we determine the intensity of shaking I, as defined by the Modified Mercalli Intensity Scale (see Table 2), the most widely-used intensity scale developed over the last several hundred years to evaluate the effects of earthquakes. We achieve this by defining an "effective seismic magnitude" as the magnitude of an earthquake centered at our specified distance away from the impact that produces the same ground motion amplitude as would be produced by the impact-induced seismic shaking. We then use Table 3, after Richter (1958), to relate the effective seismic magnitude to the Modified Mercalli Intensity. A range of intensities is associated with a given seismic magnitude because the severity of shaking depends on the local geology and rheology of the ground and the propagation of teleseismic waves; for example, damage in alluviated areas will be much more severe than on well-consolidated bed rock.

The equations for effective seismic magnitude use curves fit to empirical data of ground motion as a function of distance from earthquake events in California (Richter 1958, p. 342). We use three functional forms to relate the effective seismic magnitude M_{eff} to the actual seismic magnitude M and the distance from the impact site r_{km} (in km), depending on the distance away from the impact site. For r_{km} <60 km:

$$M_{eff} = M - 0.0238r_{km} \qquad (41a^*)$$

for 60 ≤r_{km} <700 km:

$$M_{eff} = M - 0.0048r_{km} - 1.1644 \qquad (41b^*)$$

and for r_{km} ≥700 km:

$$M_{eff} = M - 1.66\log_{10}\Delta - 6.399 \qquad (41c^*)$$

To compute the arrival time T_s of the most violent seismic shaking, we assume that the main seismic wave energy is that associated with the surface waves. Then, T_s is simply the user-specified distance r_{km} (in km) divided by the typical surface-wave velocity of upper-crustal rocks (~5 km s^{-1}):

$$T_s = \frac{r_{km}}{5} \qquad (42^*)$$

Table 3. Abbreviated version of the Modified Mercalli Intensity scale.

Intensity	Description
I	Not felt except by a very few under especially favorable conditions.
II	Felt only by a few persons at rest, especially on upper floors of buildings.
III	Felt quite noticeably by persons indoors, especially on upper floors of buildings. Many people do not recognize it as an earthquake. Standing motor cars may rock slightly. Vibrations similar to the passing of a truck.
IV	Felt indoors by many, outdoors by few during the day. At night, some awakened. Dishes, windows, doors disturbed; walls make cracking sound. Sensation like heavy truck striking building. Standing motor cars rocked noticeably.
V	Felt by nearly everyone; many awakened. Some dishes, windows broken. Unstable objects overturned. Pendulum clocks may stop.
VI	Felt by all, many frightened. Some heavy furniture moved; a few instances of fallen plaster. Damage slight.
VII	Damage negligible in buildings of good design and construction; slight to moderate in well-built ordinary structures; considerable damage in poorly built or badly designed structures; some chimneys broken.
VIII	Damage slight in specially designed structures; considerable damage in ordinary substantial buildings with partial collapse. Damage great in poorly built structures. Fall of chimneys, factory stacks, columns, monuments, and walls. Heavy furniture overturned.
IX	General panic. Damage considerable in specially designed structures; well-designed frame structures thrown out of plumb. Damage great in substantial buildings, with partial collapse. Buildings shifted off foundations. Serious damage to reservoirs. Underground pipes broken. Conspicuous cracks in ground. In alluviated areas sand and mud ejected, earthquake fountains, sand craters.
X	Most masonry and frame structures destroyed with their foundations. Some well-built wooden structures and bridges destroyed. Serious damage to dams, dikes, and embankments. Large landslides. Water thrown on banks of canals, rivers, lakes, etc. Sand and mud shifted horizontally on beaches and flat land. Rails bent slightly.
XI	As X. Rails bent greatly. Underground pipelines completely out of service.
XII	As X. Damage nearly total. Large rock masses displaced. Lines of sight and level distorted. Objects thrown into the air.

EJECTA DEPOSIT

During the excavation of the crater, material originally situated close to the target surface is either thrown out of the crater on ballistic trajectories and subsequently lands to form the ejecta deposit, or is merely displaced upward and outward to form part of the crater rim. This uplifted portion of the crater-rim material is significant close to the transient crater rim but decreases rapidly with distance such that, outside two transient-crater radii from the crater center, the material above the pre-impact target surface is almost all ejecta deposit. For simplicity, we ignore the uplifted fraction of the crater rim material. We estimate the thickness of ejecta at a given distance from an impact by assuming that the material lying above the pre-impact ground surface is entirely ejecta, that it has a maximum thickness $t_e = h_{tr}$ at the transient crater rim, and that it falls off as one over the distance from the crater rim cubed:

$$t_e = \frac{h_{tr}}{8}\left(\frac{d_{tr}}{r}\right)^3 \tag{43}$$

The power of −3 is a good approximation of data from explosion experiments (McGetchin et al. 1973) and a satisfactory compromise for results from numerical calculations of impacts and shallow-buried nuclear explosions, which show that the power can vary between −2.5 and −3.5.

The ejecta thickness at the transient crater rim (assumed to be equal to the transient crater rim height h_{tr}) may be calculated from a simple volume conservation argument where we equate the volume of the ejecta deposit and uplifted transient crater rim V_e with the volume of the transient crater below the pre-impact surface V_{tc}. For this simple model, we assume that the transient crater is a paraboloid with a depth to diameter ratio of $1{:}2\sqrt{2}$. V_e is given by:

$$V_e = \frac{h_{tr}D_{tr}^3}{8}\int_{D_{tr}/2}^{\infty}\frac{2\pi r\,dr}{r^3} + \int_{D_{tc}/2}^{D_{tr}/2} 2\pi r\left(\frac{4d_{tc}}{D_{tc}^2}r^2 - d_{tc}\right)dr$$

$$= \frac{\pi}{2}\left(h_{tr}D_{tr}^2 + d_{tc}\left[\frac{D_{tr}^4 - D_{tc}^4}{4D_{tc}^2} - \frac{D_{tr}^2 - D_{tc}^2}{2}\right]\right) \tag{44}$$

where D_{tr} is the diameter of the transient crater at the transient crater rim (see Fig. 3a), which is related to D_{tc} by:

$$D_{tr} = D_{tc}\sqrt{\frac{d_{tc} + h_{tr}}{d_{tc}}} \tag{45}$$

The volume of the transient crater is given by:

$$V_{tc} = \frac{\pi D_{tc}^3}{16\sqrt{2}} \tag{46}$$

Equating V_e with V_{tc} and rearranging to find the rim height gives $h_{tr} = D_{tc}/14.1$. Inserting this result into Equation 43 gives the simple expression used in the program:

$$t_e = \frac{D_{tc}^4}{112r^3} \tag{47*}$$

As this model ignores any "bulking" of the ejecta deposit and entrainment of the substrate on which the ejecta lands, it provides a lower bound on the probable ejecta thickness. The use of transient crater diameter instead of final crater diameter avoids the need for a separate rim height equation for simple and complex craters. Rim heights of complex craters, as a fraction of the final crater diameter, are significantly smaller than the scaled rim heights of simple craters because, for complex craters, the thickest part of the ejecta blanket collapses back into the final crater during the late stages of the cratering process. As this collapse process is not fully understood, we only report the ejecta thickness outside the final crater rim. The final rim height of the crater, which is required for our estimate of the breccia-lens thickness in simple craters (above) is found by inserting r = D_{fr}/2 into Equation 31:

$$h_{fr} = 0.07\frac{D_{tc}^4}{D_{fr}^3} \quad (48^*)$$

The outward flight of rock ejected from the crater occurs in a transient, rarefied atmosphere within the expanding fireball. In large impacts (E >200 Mt), the fireball radius is comparable to the scale height of the atmosphere; hence, the ejecta's trajectory takes it out of the dense part of the atmosphere, allowing it to reach distances much in excess of the fireball radius. For smaller impacts, however, the ejecta's outward trajectory is ultimately stifled at the edge of the fireball, where the atmospheric density returns to normal. We incorporate these considerations into our program by limiting the spatial extent of the ejecta deposit to the range of the fireball for impact energies less than 200 Mt.

The ejecta arrival time is determined using ballistic travel time equations derived by Ahrens and O'Keefe (1978) for a spherical planet. Using a mean ejection angle of 45° to the Earth's surface allows us to estimate the approximate arrival time of the bulk of the ejecta. In reality, material is ejected from the crater at a range of angles, and consequently, the arrival of ejecta at a given location does not occur simultaneously. However, this assumption allows us to write down an exact (although complex) analytical expression for the average travel time of the ejecta T_e to our specified location:

$$T_e = \frac{2a^{1.5}}{\sqrt{g_E R_E^2}}\left[2\tan^{-1}\left(\sqrt{\frac{1-e}{1+e}}\tan\frac{\Delta}{4}\right) - \left(\frac{e\sqrt{1-e^2}\sin(\Delta/2)}{1+e\cos(\Delta/2)}\right)\right] \quad (49^*)$$

where R_E is the radius of the Earth, g_E is the gravitational acceleration at the surface of the Earth, and Δ is the epicentral angle between the impact point and the point of interest. The ellipticity e of the trajectory of ejecta leaving the impact site at an angle of 45° to the horizontal and landing at the point of interest is given by:

$$e^2 = \frac{1}{2}\left[\left(\frac{v_e^2}{g_E R_E} - 1\right)^2 + 1\right] \quad (50^*)$$

where v_e is the ejection velocity, and e is negative when $v_e^2/g_E R_E \leq 1$. The semi-major axis a of the trajectory is given by:

$$a = \frac{v_e^2}{2g_E(1-e^2)} \quad (51^*)$$

To compute the ejection velocity of material reaching the specified range $r = \Delta R_E$, we use the relation:

$$v_e^2 = \frac{2g_E R_E \tan\Delta/2}{1+\tan\Delta/2} \quad (52^*)$$

which assumes that all ejecta is thrown out of the crater from the same point and at the same angle (45°) to the horizontal.

Equation 49 is valid only when $v_e^2/g_E R_E \leq 1$, which corresponds to distances from the impact site less than about 10,000 km (1/4 of the distance around the Earth). For distances greater than this, a similar equation exists (Ahrens and O'Keefe 1978); however, we do not implement it in our program because, in this case, the arrival time of the ejecta is much longer than one hour. Consequently, an accurate estimate of ejecta thickness at distal locations must take into account the rotation of the Earth, which is beyond the scope of our simple program. Furthermore, ejecta traveling along these trajectories will be predominantly fine material that condensed out of the vapor plume and will be greatly affected by reentry into the atmosphere, which is also not considered in our current model. For ejecta arrival times longer than one hour, therefore, the program reports that "little rocky ejecta reaches our point of interest; fallout is dominated by condensed vapor from the impactor."

We also estimate the mean fragment size of the fine ejecta at our specified location using results from a study of parabolic ejecta deposits around venusian craters (Schaller and Melosh 1998). These ejecta deposits are thought to form by the combined effect of differential settling of fine ejecta fragments through the atmosphere depending on fragment size (smaller particles take longer to drop through the atmosphere), and the zonal winds on Venus (Vervack and Melosh 1992). Schaller and Melosh (1998) compared a theoretical model for the formation of the parabolic ejecta deposits with radar observations and derived an empirical law for the mean diameter of impact ejecta d (in m) on Venus as a function of distance from the crater center r_{km} (in km):

$$d = d_c\left(\frac{D_{fr}}{2r_{km}}\right)^{\alpha} \quad (53^*)$$

where D_{fr} is the final crater diameter measured from rim to rim (in km); $\alpha = 2.65$, and $d_c = 2400(D_{fr}/2)^{-1.62}$. This relation neglects the effects of the atmosphere and wind transportation on Earth, which will be more significant for

smaller fragment sizes, and the disintegration of ejecta particles as they land. Thus, the uncertainty in these predictions is greatest very close to the crater, where ejecta fragments are large and will break up significantly during deposition, and at great distances from the impact point, where the predicted fragment size is small. We circumvent this problem at small distances by not calculating the mean fragment size for ranges less than two crater radii, which roughly corresponds to the extent of the continuous ejecta blanket observed around extra-terrestrial craters (Melosh 1989, p. 90). We also emphasize that the predicted fragment size is a rough mean value of the ejecta fragment size. At any given location, there will be a range of fragment sizes around this mean including large bombs and very fine-grained dust, which will arrive at different times depending on how easily they traverse the atmosphere.

AIR BLAST

The impact-induced shock wave in the atmosphere is referred to as the air blast or blast wave. The intensity of the blast depends on the energy released during the impact and the height in the atmosphere at which the energy is deposited, which is either zero for impacts where a crater is formed or the burst altitude for airburst events. The effects of the blast wave may be estimated by drawing on data from US nuclear explosion tests (Glasstone and Dolan 1977; Toon et al. 1994, 1997; Kring 1997). The important quantities to determine are the peak overpressure, that is, the maximum pressure in excess of the ambient atmospheric pressure (1 bar = 10^5 Pa), and the ensuing maximum wind speed. With these data, tables compiled by the US Department of Defense may be used to predict the damage to buildings and structures of varying constructional quality, vehicles, windows, and trees.

To estimate the peak overpressure for crater-forming impacts, we assume that the impact-generated shock wave in the air is directly analogous to that generated by an explosive charge detonated at the ground surface (surface burst). We found that the expression:

$$p = \frac{p_x r_x}{4 r_1}\left(1 + 3\left(\frac{r_x}{r_1}\right)^{1.3}\right) \quad (54^*)$$

is an excellent fit to empirical data on the decay of peak overpressure p (in Pa) with distance r_1 (in m) for a 1 kiloton (kt) surface burst (Glasstone and Dolan 1977; their Fig. 3.66, p. 109). In this equation, the pressure p_x at the crossover point from $\sim 1/r^{2.3}$ behavior to $\sim 1/r$ behavior is 75000 Pa (0.75 bars); this occurs at a distance of 290 m.

The peak overpressure resulting from an airburst is estimated using a similar suite of equations fit to empirical data on the peak overpressure experienced at different distances away from explosions detonated at various heights above the surface (Glasstone and Dolan 1977, p. 113). The relationship between peak overpressure and distance away from ground zero (the location on the Earth directly below the airburst) is more complex than for a surface burst due to the interaction between the blast wave direct from the source and the wave reflected off the surface. Within a certain distance from ground zero, the delay between the arrival of the direct wave and the reflected wave is sufficient for little constructive interference of the waves to occur; this region is known as the regular reflection region. Beyond this zone, however, the two waves merge in what is known as the "Mach reflection region;" this effect can increase the overpressure at a given location by as much as a factor of two (Glasstone and Dolan 1977, p. 38). Within the Mach region, we found that Equation 54 holds approximately, provided that the crossover distance r_x is increased slightly as a function of burst altitude ($r_x = 289 + 0.65 z_b$). At distances inside the regular reflection region, we found that the peak overpressure decreases exponentially with distance from ground zero:

$$p = p_0 e^{-\beta r_1} \quad (55^*)$$

where p_0 and β are both functions of burst altitude:

$$p_0 = 3.14 \times 10^{11} z_b^{-2.6} \quad (56a^*)$$

$$\beta = 34.87 z_b^{-1.73} \quad (56b^*)$$

To extrapolate these relationships to explosions (impacts) of greater energy, we again rely on yield scaling, which implies that a specific peak overpressure occurs at a distance from an explosion that is proportional to the cube root of the yield energy. In other words, the ratio of the distance at which a certain peak overpressure occurs to the cube root of the impact energy ($r(p)/E^{1/3}$) is constant for all impacts. Therefore, the peak overpressure at the user-specified distance r away from an impact of energy E_{kt} (in kilotons) is the same as that at a distance r_1 away from an impact of energy 1 kt, where r_1 is given by:

$$r_1 = \frac{r}{E_{kT}^{1/3}} \quad (57^*)$$

The equivalent burst altitude in a 1 kt explosion z_{b1} is related to the actual burst altitude by a similar equation $z_{b1} = z_b / E_{kt}^{1/3}$.

To compute the peak overpressure, we substitute the scaled-distance r_1 into Equation 54 or 55, depending on whether the distance r_1 lies within the Mach region or the regular reflection region for a 1 kt explosion. The distance from ground zero to the inner edge of the Mach region r_{m1} in such an explosion depends only on the altitude of burst z_{b1}; we found a good fit to the observational data with the simple function:

$$r_{m1} = \frac{550 z_{b1}}{1.2(550 - z_{b1})} \quad (58^*)$$

Table 4. Air blast damage.[a]

Distance from a 1 kt explosion (d_1 in m)	Over pressure (p in Pa)	Description of air blast-induced damage
126	426000	Cars and trucks will be largely displaced and grossly distorted and will require rebuilding before use.
133	379000	Highway girder bridges will collapse.
149	297000	Cars and trucks will be overturned and displaced, requiring major repairs.
155	273000	Multistory steel-framed office-type buildings will suffer extreme frame distortion, incipient collapse.
229	121000	Highway truss bridges will collapse.
251	100000	Highway truss bridges will suffer substantial distortion of bracing.
389	42600	Multistory wall-bearing buildings will collapse.
411	38500	Multistory wall-bearing buildings will experience severe cracking and interior partitions will be blown down.
502	26800	Wood frame buildings will almost completely collapse.
549	22900	Interior partitions of wood frame buildings will be blown down. Roof will be severely damaged.
1160	6900	Glass windows shatter.

[a]Data extracted from Glasstone and Dolan (1977).

Note that for surface bursts ($z_{b1} = 0$), the Mach region is assumed to begin at the impact point ($r_{m1} = 0$); for scaled burst-altitudes in excess of 550 m, there is no Mach region. The calculated peak overpressure can then be compared with data presented in Table 4 to assess the extent of the air blast damage.

The characteristics of a blast wave in air at the shock front are uniquely related by the Hugoniot equations when coupled with the equation of state for air. The particle velocity (or peak wind velocity) behind the shock front u is given by:

$$u = \frac{5p}{7P_0} \frac{c_0}{(1 + 6p/7P_0)^{0.5}} \quad (59^*)$$

where P_0 is the ambient pressure (1 bar), c_0 is the ambient sound speed in air (~330 m s^{-1}), and p is the overpressure (Glasstone and Dolan 1977, p. 97). If the calculated maximum wind velocity is greater than 40 m s^{-1}, experience from nuclear weapons tests suggests that "about 30% of trees are blown down; the remainder have some branches and leaves blown off" (Glasstone and Dolan 1977, p. 225). If the maximum wind velocity is greater than 62 m s^{-1}, devastation is more severe: "Up to 90 percent of trees blown down; remainder stripped of branches and leaves."

The blast wave arrival time is given by:

$$T_b = \int_0^r \frac{dr}{U(r)} \quad (62)$$

where U is the shock velocity in air, given formally by:

$$U(r) = c_0 \left(1 + \frac{6p(r)}{7P_0}\right)^{0.5} \quad (63)$$

For convenience, however, we assume that the shock wave travels at the ambient sound speed in air c_0. In this case, the air blast arrival time at our specified distance r is simply:

$$T_b = \frac{r}{c_0} \quad (64^*)$$

This simplification results in large errors only very close to the crater rim.

The air blast model we use extrapolates from data recorded after a very small explosion (in impact cratering terms) in which the atmosphere may be treated as being of uniform density. Furthermore, at this scale of explosion, the peak overpressure decays to zero at distances so small (<1 km) that the curvature of the Earth may be ignored. Neither of these assumptions applies to larger impacts; thus, the reliability of our predictions decreases as impact energy increases. In the future, we hope to examine the effect of a variable-density atmosphere and a curved Earth on the blast wave decay using numerical modeling. Such sophisticated calculations of the interaction between a hot ejecta plume and a realistic atmosphere by Zahnle (1990) and Toon et al. (1994), which included blast wave formation, are in good agreement with our simple model in the 1–10000 Mt range; for impact energies greater than this, Equation 44 probably overestimates the blast wave effects by a factor of 2–5.

EFFECT OF A WATER LAYER

The rationale discussed above for predicting the environmental consequences of an asteroid collision with Earth assumes that the impact occurs on land. In fact, marine impacts are more than twice as likely to occur as land impacts on Earth. The influence of a water layer on the impact process has been the subject of many recent field studies (Tsikalas et

al. 1998, 1999; Ormö and Lindström 2000), laboratory experiments (McKinnon and Goetz 1981; Gault and Sonnett 1982), and numerical simulations (O'Keefe and Ahrens 1982a; Roddy et al. 1987; Ormö and Miyamoto 2002; Shuvalov et al. 2002; Artemieva and Shuvalov 2002; Wünnemann and Lange 2002), which have led to a qualitative paradigm for submarine cratering in both the deep ocean (Wünnemann and Lange 2002) and shallow seas (Oberbeck et al. 1993; Poag et al. 2004). However, like many other aspects of impact cratering, an accurate quantitative treatment of the effect of a water layer on the cratering process requires complicated numerical methods beyond the scope of our program. Consequently, our program employs only a rudimentary algorithm for estimating the effect of a water column on the environmental consequences of an impact. We estimate the change in velocity of the impactor at the seafloor $v_i|_{seafloor}$ from that at the surface $v_i|_{surface}$ by integrating the drag equation (Equation 7) over the depth of the water column:

$$v_i\big|_{seafloor} = v_i\big|_{surface} \exp\left\{-\frac{3\rho_w C_D d_w}{2\rho_i L \sin\theta}\right\} \qquad (65^*)$$

In this equation, d_w is the thickness of the water layer, L is the diameter of the impactor after the atmospheric traverse, and C_D is the drag coefficient for a rigid sphere of water in the supersonic regime, which we set equal to 0.877 (Landau and Lifshitz 1959). This simple expression ignores both the flattening of the impactor during penetration and the propagation of the shock wave through the water column; however, it agrees quite favorably with numerical simulations of deep sea impact events (Wünnemann and Lange 2002).

For marine impact scenarios, we calculate the approximate kinetic energy of the impactor at the moment it strikes the surface of the water layer $E_{surface}$ and when it reaches the seafloor $E_{seafloor}$. Using Equation 16, we compute and report two transient crater diameters: one in the water layer and one in the seafloor. For the transient crater diameter in the water layer, we use the impact velocity at the surface ($v_i = v_i|_{surface}$), replace the constant 1.161 with 1.365, and use a target density equal to the density of water ($\rho_t = \rho_w = 1000$ kg m^{-3}). For the transient crater diameter in the seafloor we assume that the impact velocity is that of the impactor at the seafloor ($v_i = v_i|_{seafloor}$) and use a target density of $\rho_t = 2700$ kg m^{-3}.

From this point, the program continues as before, calculating the dimensions of the crater in the seafloor, whether it is simple or complex, the volume of the target below the seafloor that is melted, etc. The air blast and thermal radiation calculations proceed assuming that the impact energy is that released at the surface of the water layer ($E = E_{surface}$); the seismic shaking and ejecta calculations, on the other hand, assume that the impact energy is the kinetic energy of the impactor at the moment it reaches the sea floor ($E = E_{seafloor}$). As a result, our program predicts that the thermal radiation and air blast effects are unchanged by the presence of the water column relative to a land impact of the same energy. However, a deep enough water layer could entirely suppress the seismic shaking and excavation of rocky ejecta that would occur in an impact of the same size on dry land.

The current version of the program does not compute the effects of impact-generated tsunamis for water impacts. There are several reasons for this omission, in spite of requests by many users for this feature. The first set of reasons is practical. A plausible tsunami computation requires not only the depth of the water at the impact site, but also the depth of the ocean over the entire path from the impact to the observer. The observer must, of course, be on a coastline with an unobstructed great circle path to the impact site. The observed tsunami height and run up depends on the local shoreline configuration and slope, the presence or absence of offshore bars, etc. The sheer number of input parameters required would daunt most potential users. This sort of computation requires a professional effort of the scale of Ward and Asphaug (2000, 2003); it is far beyond the capability of our simple program. The other set of reasons centers around the current uncertainty of the size of tsunamis generated by impacts. Following some initial spectacular estimates of tsunami heights, heights that greatly exceed the depth of the ocean itself (Hills et al. 1994), a reaction occurred (Melosh 2003) based on a newly-unclassified document (Van Dorn et al. 1968) that suggests that impact-tsunami waves break on the continental shelf and pose little threat to coastal locations (the "Van Dorn" effect). The present situation with regard to this hazard is thus confused, and we decided against including such an estimate in our code until the experts have sorted out the actual size of the effect.

GLOBAL EFFECTS

In addition to the regional environmental consequences of the impact event, we also compute some global implications of the collision. We compare the linear momentum of the impactor at the moment it strikes the target surface, $M_i = m_i v_i$, with the linear momentum of the Earth, $M_E = m_E v_E$, where m_E is the mass of the Earth (5.83×10^{24} kg) and v_E is the mean orbital velocity of the Earth (29.78 km s^{-1}). Depending on the ratio M_i/M_E, the program reports the likely effect of the impact on the orbit of the Earth. Our choice of limits on M_i/M_E and the corresponding degree to which the orbit changes is presented in Table 5. We compare the angular momentum imparted by the impact $\Gamma_i = m_i v_i R_E \cos\theta$ to the angular momentum of the Earth $\Gamma_E = 5.86 \times 10^{33}$ kg m^3 s^{-1} in a similar manner. Table 5 also presents the ranges of the ratio Γ_i/Γ_E for which we assume certain qualitative changes to the Earth's rotation period and the tilt of its axis as a result of the impact. Finally, we compare the volume of the transient crater V_{tc} with the volume of the Earth V_E. In the event that the ratio

V_{tc}/V_E is greater than 0.5, we assume that the Earth is completely disrupted by the impact and forms a new asteroid belt between Venus and Mars. If V_{tc}/V_E is in the range of 0.1–0.5, the program reports that the Earth is strongly disturbed by the impact but loses little mass. Otherwise, the program reports that the Earth is not strongly disturbed by the impact and loses negligible mass.

Currently, we do not make any estimates regarding the potentially global environmental consequences of large impact events. In such catastrophes, dust, melt droplets, and gas species generated during the impact event are ejected out of the Earth's atmosphere and dispersed all over the globe (Alvarez 1980). Several potentially devastating environmental consequences could result from the re-entry and prolonged settling though the atmosphere of this material (Toon et al. 1982, 1994, 1997; Zahnle 1990; Kring 2000). Thermal radiation generated during the re-entry of high speed ejecta may be strong enough to ignite wildfires over large areas of the globe (Alvarez 1980; Melosh et al. 1990; Toon et al. 1994, 1997). Dust loading in the atmosphere may block out light and restrict photosynthesis for months after the impact (Toon et al. 1982, 1994, 1997; Covey et al. 1990; Zahnle 1990). Furthermore, the presence of carbonate or anhydrite rocks in the sedimentary target sequence may add additional environmental consequences due to the production of climatically active gas species (Lewis et al. 1982; Prinn and Fegley 1987; Zahnle 1990; Brett 1992; Pope et al. 1997; Pierazzo et al. 1998; Kring 1999). These compounds may produce aerosols that further reduce the amount of light that reaches the surface of the Earth, condense with water to form acid rain, react with and deplete ozone levels, and cause "greenhouse" warming. To make reasonable estimates of the severity of these effects requires detailed, time-consuming computations involving a large suite of model parameters (for example, target chemistry and mass-velocity distributions for the ejected material; Toon et al. 1997). Such calculations are well beyond the scope of our simple program; we direct readers interested in these processes to the above references for further information.

APPLICATIONS OF THE EARTH IMPACT EFFECTS PROGRAM

We have written a computer program that estimates the environmental consequences of impact events both past and future using the analytical expressions presented above. To illustrate the utility of our program, consider the hypothetical devastation at various locations within the United States if asteroids of various sizes were to strike Los Angeles. The first event worthy of consideration is the impact of a ~75-m diameter stony asteroid (density = 2000 kg m^{-3}), which occurs somewhere on earth every 900 years on average. In this case, our program determines that the impactor would begin to disrupt at an altitude of ~66 km and deposit the majority of its kinetic energy in the atmosphere at a burst altitude of ~5 km. The air blast from this event would be strong enough to cause substantial damage to wooden buildings and blow down 90% of trees to a radius of ~15 km, which agrees well with the extent of forest damage observed after the Tunguska airburst event in Siberia in 1908.

Table 5. Global implications of an impact event.

Ratio	Qualitative global change
$M_i/M_E < 0.001$	No noticeable change in orbit.
$0.001 < M_i/M_E < 0.01$	Noticeable change in orbit.
$0.01 < M_i/M_E < 0.1$	Substantial change in orbit.
$M_i/M_E > 0.1$	Totally changes orbit.
$\Gamma_i/\Gamma_E < 0.01$	No noticeable change in rotation period and tilt of axis.
$0.01 < \Gamma_i/\Gamma_E < 0.1$	Noticeable change in rotation period and tilt of axis.
$0.1 < \Gamma_i/\Gamma_E < 1.0$	Substantial change in rotation period and tilt of axis.
$\Gamma_i/\Gamma_E > 1.0$	Totally changes rotation period and tilt of axis.

Next, let us examine the environmental consequences of three impact events of drastically different magnitudes at a fixed distance of 200 km away from our impact site in Los Angeles, which is the approximate distance from L.A. to San Diego. The three impacts we will consider are a 40-m diameter iron asteroid (density = 8000 kg m^{-3}) impacting at 20 km s^{-1} into a sedimentary target (density = 2500 kg m^{-3}), which is the approximate scenario of the event that formed Barringer Crater in northern Arizona; a 1.75-km diameter stony asteroid (density = 2700 kg m^{-3}) impacting at 20 km s^{-1} into a crystalline target (density = 2750 kg m^{-3}), which corresponds approximately to the magnitude of the impact event that formed the Ries crater in Germany; and an 18-km diameter stony asteroid also impacting at 20 km s^{-1} into a crystalline target, which represents a reasonable estimate of the scale of the Chicxulub impact event in the Gulf of Mexico. For each impact we assume identical impact angles ($\theta = 45°$). Table 6 presents a comparison of the important parameters discussed in this paper for each impact event at a distance of 200 km away from our hypothetical impact center in Los Angeles. Note the substantial variation in impact energy between each impact event, which results in very different estimated environmental effects 200 km away in San Diego. The average recurrence interval is for the entire Earth; the two larger impact scenarios are both extremely rare events. All of these impactors are large enough (or strong enough) to traverse the atmosphere and create a single impact crater; however, the Barringer-scale impactor is slowed considerably by the atmosphere.

In the case of the small iron asteroid impact, San Diego is a very safe place to be. As little to no vapor is generated during this event, there is no significant thermal radiation. The impact crater formed is only 1.2 km in diameter; the atmosphere would prevent much if any ejecta thrown out of

Table 6. Comparison of environmental effects 200 km away from various impacts.

Impactor size (km)		0.04 (iron)	1.75	18
Percentage reduction in velocity during atmospheric entry	Equations 9, 11, 12, 15, 16, 17, 20	50	–	–
Impact energy (J) (megatons; 1 Mt = 4.2×10^{15} J)	Equation 1	1.3×10^{16} 3.2	1.5×10^{21} 3.6×10^{5}	1.65×10^{24} 3.9×10^{8}
Recurrence interval (years; whole Earth)	Equation 3	1000[a]	2.1×10^{6}	4.6×10^{8}
Final crater diameter (km)	Equations 21 and 22 or 27	1.2 (Simple)	23.7 (Complex)	186 (Complex)
Fireball radius (km)	Equation 32	–	23	236
Time at which radiation begins (s)	Equation 33	–	1.2	–
Thermal exposure (MJ m^{-2})	Equation 34, 36, 37	–	14.8	–
Duration of irradiation (s)	Equation 35	–	300	–
Thermal radiation damage	Equation 39; Table 1	No fireball created due to low impact velocity.	Third degree burns; many combustible materials ignited.	Within the fireball radius, everything incinerated!
Arrival time of major seismic shaking (s)	Equation 42	40	40	40
Richter scale magnitude	Equation 40	4.9	8.3	10.4
Modified Mercalli Intensity	Equation 41; Tables 2 and 3	I–II (III)[b]	VII–VIII (VIII)[b]	X–XI (XI)[b]
Arrival time of bulk ejecta (s)	Equations 49–52	Ejecta blocked by atmosphere.	206	206
Average ejecta thickness (m)	Equation 47	–	.09	137
Mean fragment diameter (cm)	Equation 53	–	2.4	–
Arrival time of air blast (s)	Equation 64	606	606	606
Peak overpressure (bars)	Equations 54 and 57	0.004	0.80	77
Maximum wind velocity (m/s)	Equation 59	0.96	145	2220
Air blast damage	Table 4	Blast pressure insufficient to cause damage.	Wooden and tall unstable buildings collapse; glass windows shatter; 90% trees blown down.	Collapse of almost all buildings and bridges; damage and overturning of vehicles; 90% of trees blown down.

[a]Note that the recurrence interval is based on impact energy alone. Iron asteroids represent only ~5% of the known NEOs; therefore, the real recurrence interval for an impact of this sort is ~20 times longer.

[b]Estimates of seismic intensity according to Toon et al. (1997).

the crater from reaching San Diego. Furthermore, the air blast would be extremely weak at a radius of 200 km: the change in atmospheric pressure would be barely discernible at a rise of less than one part in a hundred with ensuing wind speeds of under a meter per second. The only noticeable consequences from this scale of impact would be from seismic shaking, which would be most obvious around 40 sec after the impact occurred. The impact would be analogous to an earthquake of Richter magnitude 4.9 centered in L.A. The Modified Mercalli Intensity of the shaking in San Diego would be in the range of I–II, depending on the local geology, meaning that the disturbance would be felt only in favorable circumstances and would not cause any permanent damage.

In stark contrast, San Diego would not be an attractive location in the event that either of the two larger impacts occurred in L.A. In the case of a 1.75-km diameter asteroid impact, the thermal exposure at a range of 200 km would be sufficient to ignite most combustible materials and cause third degree burns to unfortunate San Diegans, particularly if visibility was good. The seismic surface waves emanating from the impact site would arrive half a minute later and would be violent enough to damage poorly constructed structures, topple tall chimneys, factory stacks, and monuments, and overturn furniture in homes and offices. A relatively thin layer of ejecta would arrive a few minutes after the impact and begin to rain down through the atmosphere covering the city in a few cm of ejecta fragments. During this time, the air blast wave would propagate across the city flattening any poorly constructed structure that remained standing and kicking up 150 m/s winds capable of blowing over most trees.

In the case of a Chicxulub-scale event, the environmental consequences in San Diego would be extreme. Seconds after the impact, the fireball would engulf the city of San Diego, incinerating all combustible materials. The seismic shaking that would arrive moments later would be as violent as that caused by the most severe earthquake recorded on Earth. If anything remained standing after this episode, it would soon be smothered and suffocated by the arrival of a huge amount of rock debris thrown out of the growing crater. Finally, a

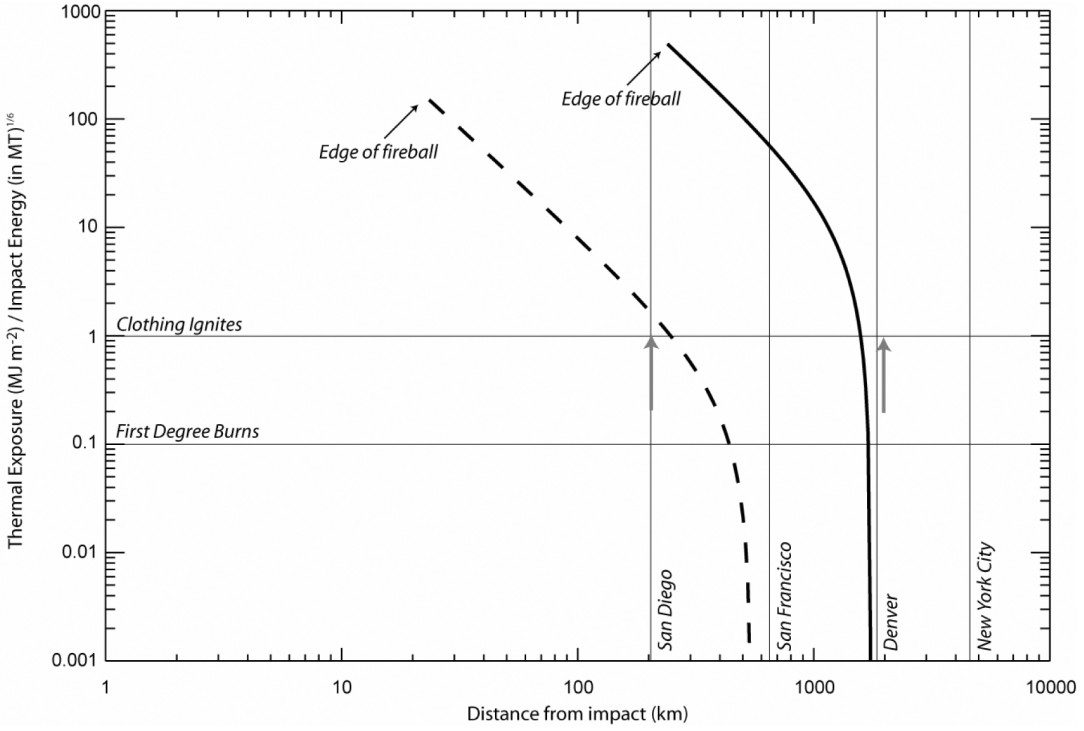

Fig. 4. Thermal exposure from the impact-generated fireball, divided by the impact energy (in Mt) to the one-sixth power, as a function of distance from the impact center, for three hypothetical impacts in Los Angeles. (Dividing $f\Phi$ by $E_{Mt}^{1/6}$ allows us to more easily compare the extent of thermal radiation damage for impacts of different energies. Plotted in this way, the scaled thermal exposure required to ignite a given material does not depend on impact energy; thus, values on the ordinate can be compared directly with the data in Table 1.) The solid line represents an impact of an 18-km diameter stony asteroid; the dashed line represents an impact of a 1.75-km stony asteroid; no line appears for the 40-m iron asteroid because little to no vapor is produced during the impact and no significant thermal radiation occurs. The vertical lines represent four distances from the impact center that correspond to the approximate distances from L.A. to four major U.S. cities. Grey arrows indicate the radial extent of fires ignited by thermal radiation from the fireball as predicted by Toon et al. (1997). See the text for further details.

strong pressure wave nearly 80 times greater than atmospheric pressure would pass through San Diego flattening any remaining erect buildings; winds over 2 km per second would follow, violently scattering debris and ripping up trees.

The algorithm presented in this paper also allows us to extend our study of potential impact-related disasters over a range of distances away from the impact. Figures 4–7 illustrate how each of the major environmental consequences depends on the distance away from the impact site for the three different scales of impact; in each figure, the dotted line represents the 40-m diameter iron asteroid impact, the dashed line represents the 1.75-km diameter asteroid impact, and the solid line represents the 18-km diameter asteroid impact. Also marked on the figures are the approximate locations of four major U.S. cities with respect to Los Angeles, the location of our impact site. Figure 4 shows the reduction in thermal exposure with distance away from the edge of the fireball. The change in slope of the curves is caused by the curvature of the Earth, which acts to hide more and more of the fireball below the horizon with increasing distance away from the impact. As a result, the thermal radiation damage from even a Chicxulub-scale impact is restricted to a range of ~1500 km; in the event that an 18-km diameter asteroid struck L.A., Denver would probably escape any thermal radiation damage. The horizontal positions of the grey arrows in Fig. 4 denote the radial extent of thermal radiation damage for the two larger impacts, according to Toon et al. (1997). Comparing our predictions and those of Toon et al. illustrates the approximate uncertainty of both estimates. Figure 5 shows the impact ejecta thickness for each potential impact event as a function of distance. Figure 6 shows the drop in effective seismic magnitude with distance away from the impact, which can be related to the intensity of shaking using Table 2. The graph illustrates that impact-related seismic shaking would be felt by all as far as Denver if a Ries-scale impact occurred in L.A.; and significant tremors would be felt as far-a-field as New York City following a Chicxulub-scale impact in L.A. The decay in peak overpressure with distance from the impact associated with the impact air blast wave is depicted in Fig. 7. In the case of a 40-m diameter iron asteroid, the air blast damage would be confined to a few km away from the impact site. However, the blast wave from a Chicxulub-scale impact centered in L.A. may be strong enough to level steel framed buildings in San Francisco and wooden buildings as far away as Denver. For comparison, the grey squares in Fig. 7 illustrate the approximate radial extent of airblast damage for each impact event, as predicted by Toon et al. (1997). For the two larger impacts, the disagreement between

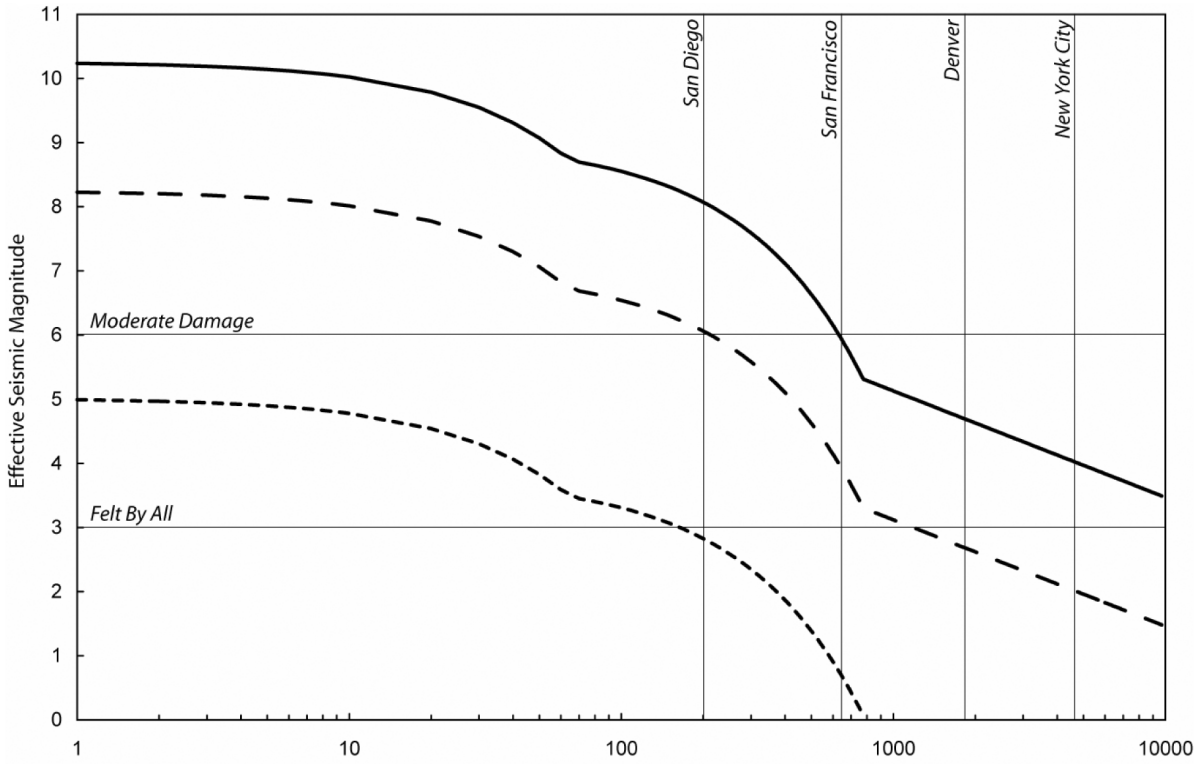

Fig. 5. The effective seismic magnitude as a function of distance away from three hypothetical impacts in Los Angeles. The solid line represents an impact of an 18-km diameter stony asteroid; the dashed line represents an impact of a 1.75-km stony asteroid; the dotted line represents the impact of a 40-m diameter iron asteroid. The vertical lines represent four distances from the impact center that correspond to the approximate distances from L.A. to four major U.S. cities. See the text for further details.

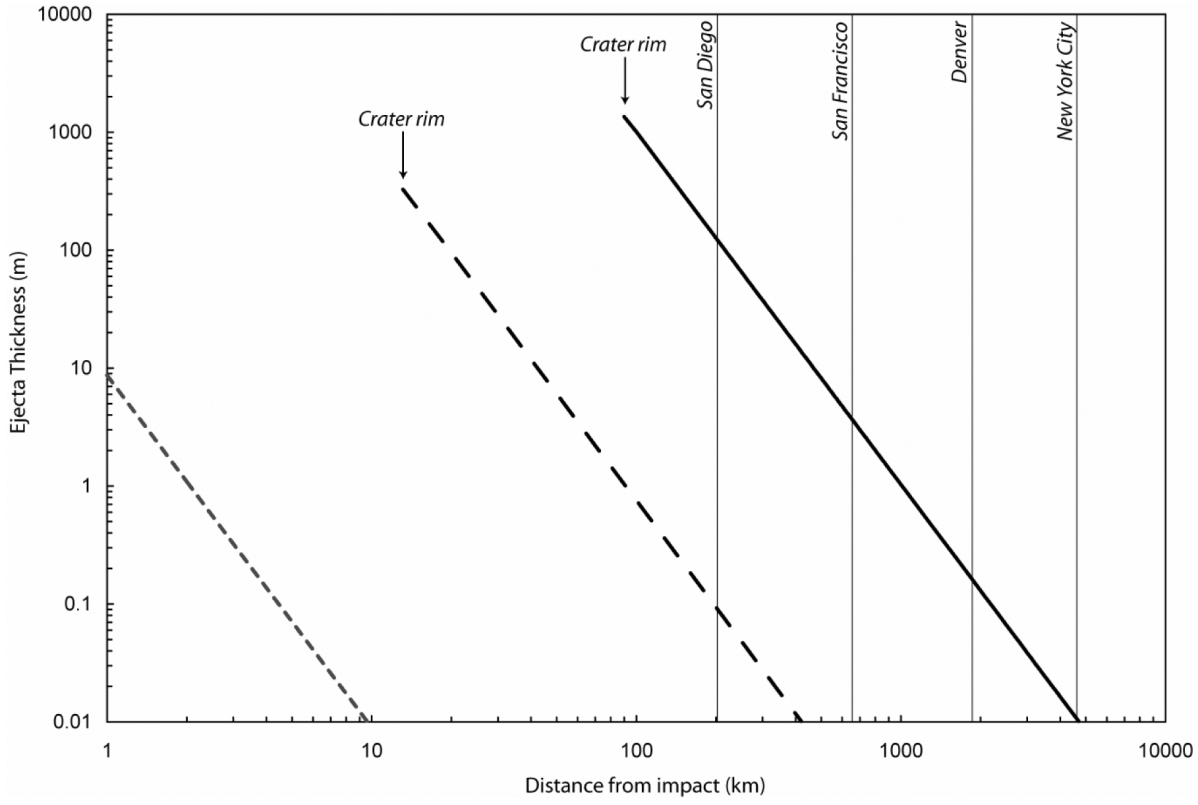

Fig. 6. The variation in ejecta-deposit thickness with increasing distance from the impact point for three hypothetical impacts centered in Los Angeles. The solid line represents an impact of an 18-km diameter stony asteroid; the dashed line represents an impact of a 1.75-km stony asteroid; the dotted line represents the impact of a 40-m diameter iron asteroid. The vertical lines represent four distances from the impact center that correspond to the approximate distances from L.A. to four major U.S. cities. See the text for further details.

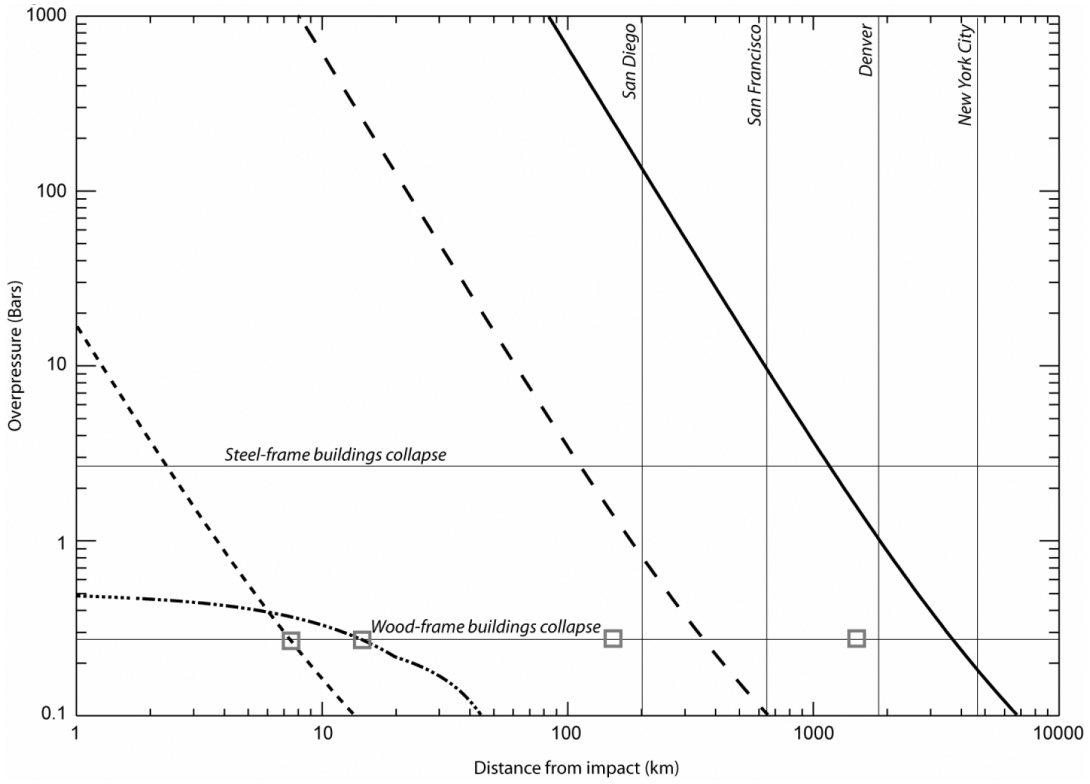

Fig. 7. The peak airblast overpressure as a function of distance from three hypothetical impacts centered in Los Angeles. The solid line represents an impact of an 18-km diameter stony asteroid; the dashed line represents an impact of a 1.75-km stony asteroid; the dotted line represents the impact of a 40-m diameter iron asteroid. The dash-dotted line illustrates the decay of peak overpressure with distance away from an airburst resulting from the impact of a 75-m diameter stony object (density = 2000 kg m^{-3}) at 17 km s^{-1}, as discussed in the text. The vertical lines represent four distances from the impact center that correspond to the approximate distances from L.A. to four major U.S. cities. The grey squares show the extent of the airblast damage as predicted by Toon et al. (1997). See the text for further details.

our predictions and those of Toon et al. (1997) is due to our neglect of the effects of Earth curvature and a variable density atmosphere, as discussed earlier.

DISCUSSION

The Earth Impact Effects Program provides a straightforward method for estimating the regional environmental consequences of the collision of extraterrestrial objects with the Earth. To implement such a program, it is necessary to make some simplifying assumptions that limit the accuracy of any predictions. Nevertheless, some important conclusions may be drawn from our simple model. Of the environmental consequences that we consider, the seismic shaking poses the most significant threat at large distances from the impact site; effects of ejecta fallout and the air blast decrease much more rapidly with distance away from the impact site. Moreover, the curvature of the Earth ensures that, even in the case of very rare ~20-km scale impact events, the thermal radiation will be confined to a maximum range of 1500 km, at which point the fireball is completely hidden below the horizon. Closer to the impact site, however, the air blast, thermal radiation, and ejecta deposition combine to severely affect the local environment and should all be considered in any hazard assessment.

We believe that we have developed a valuable tool for use both within the scientific community and the population at large. We anticipate that within the field of impact cratering our program will serve the function of providing a quick assessment of the hazard risk for potential future impact scenarios and enable those studying particular terrestrial impact events to estimate the regional environmental consequences associated with the impact. We welcome any suggestions for improvements or additions to the algorithm presented here.

Acknowledgments–Many members of the impact cratering community and users of the Earth Impact Effects Program have offered helpful advice for improvements to our model. In particular, we gratefully acknowledge input from Bevan French, Boris Ivanov, Natasha Artemieva, Ivan Nemtchinov, Kai Wünnemann, Lori Styles, Al Harris, Alexander Reid, and Blake Morlock. We are indebted to the thorough and insightful reviews of Erik Asphaug and an anonymous reviewer, and the editorial handling of Elisabetta Pierazzo. This work was supported by NASA grant NAG5–11493. This is IARC publication number 2005-0414.

Editorial Handling—Dr. Elisabetta Pierazzo

REFERENCES

Ahrens T. J. and O'Keefe J. D. 1978. Energy and mass distributions of impact ejecta blankets on the moon and Mercury. Proceedings, 9th Lunar and Planetary Science Conference. pp. 3787–3802.

Alvarez L. W., Alvarez W., Asaro F., and Michel H. V. 1980. Extraterrestrial cause for the Cretaceous-Tertiary extinction. *Science* 208:1095–1108.

Artemieva N. A. and Shuvalov V. V. 2002. Shock metamorphism on the ocean floor (numerical simulations). *Deep Sea Research Part II: Topical Studies in Oceanography* 49:959–968.

Binzel R. P., Lupishko D. F., Di Martino M., Whiteley R. J., and Hahn G. J. 2003. Physical properties of near-Earth objects. In *Asteroids III,* edited by Bottke W. F., Cellino A., Paolicchi P., and Binzel P. R. Tucson: The University of Arizona Press. pp. 255–271.

Bland P. A. and Artemieva N. A. 2003. Efficient disruption of small asteroids by the Earth's atmosphere. *Nature* 424:288–291.

Bottke W. F. Jr., Nolan M. C., Greenberg R., and Kolvoord R. A. 1994. Collisional lifetimes and impact statistics of near-Earth asteroids. In *Hazards due to comets and asteroids,* edited by Gehrels T. Tucson: The University of Arizona Press. pp 337–357.

Brett R. 1992. The Cretaceous-Tertiary extinction: A lethal mechanism involving anhydrite target rocks. *Geochimica et Cosmochimica Acta* 56:3603–3606.

Bus S. J. and Binzel R. P. 2002. Phase II of the small main-belt asteroid spectroscopic survey: A feature-based taxonomy. *Icarus* 158:146–177.

Chapman C. R. and Brandt J. C. 2004. *Introduction to comets,* 2nd edition. New York: Cambridge University Press.

Chyba C. F., Thomas P. J., and Zahnle K. J. 1993. The 1908 Tunguska explosion: Atmospheric disruption of a stony asteroid. *Nature* 361:40–44.

Covey C., Ghan S. J., Walton J. J., and Weissman P. R. 1990. Global environmental effects of impact-generated aerosols: Results from a general circulation model. In *Global catastrophes in Earth history,* edited by Sharpton V. S. and Ward P. D. Special Paper 247. Boulder: Geological Society of America. pp. 263–270.

Croft S. K. 1985. The scaling of complex craters. *Journal of Geophysical Research* 90:C828–C842.

Dence M. R. 1965. The extraterrestrial origin of Canadian craters. *Annual New York Academy of Science* 123:941–969.

Dence M. R., Grieve R. A. F., and Robertson P. B. 1977. Terrestrial impact structures: Principal characteristics and energy considerations. In *Impact and explosion cratering,* edited by Roddy D. J., Pepin R. O., and Merrill R. B. New York: Pergamon Press. pp 247–275.

Gault D. E. 1974. Impact cratering. In *A primer in lunar geology,* edited by Greeley R. and Shultz P. H. Moffett Field: NASA Ames Research Center. pp. 137–175.

Gault D. E. and Sonett C. P. 1982. Laboratory simulation of pelagic asteroid impact: Atmospheric injection, benthic topography, and the surface wave radiation field. In *Geological implications of impacts of large asteroid and comets on the Earth,* edited by Silver L. T. and Schultz P. H. Special Paper 190. Boulder: Geological Society of America. pp. 69–92.

Glasstone S. and Dolan P. J. 1977. *The effects of nuclear weapons,* 3rd edition. Washington D.C.: United States Department of Defense and Department of Energy.

Grieve R. A. F. and Cintala M. J. 1992. An analysis of differential melt-crater scaling and implications for the terrestrial impact record. *Meteoritics* 27:526–538.

Grieve R. A. F. and Garvin J. B. 1984. A geometric model for excavation and modification at terrestrial simple impact craters. *Journal of Geophysical Research* 89:11,561–11,572.

Grieve R. A. F., Dence M. R., and Robertson P. B. 1977. Cratering processes: As interpreted from the occurrence of impact melts. In *Impact and explosion cratering,* edited by Roddy D. J., Pepin R. O., and Merrill R. B. New York: Pergamon Press. pp 791–814.

Grieve R. A. F. and Therriault A. M. 2004. Observations at terrestrial impact structures: Their utility in constraining crater formation. *Meteoritics & Planetary Science* 39:199–216.

Herrick R. R., Sharpton V. L., Malin M. C., Lyons S. N., and Freely K. 1997. Morphology and morphometry of impact craters. In *Venus II,* edited by Bougher S. W., Hunten D. M., and Phillips R. J. Tucson: The University of Arizona Press. pp. 1015–1046.

Hills J. G., Nemchinov I. V., Popov S. P., and Teterev A. V. 1994. Tsunami generated by small asteroid impacts. In *Hazards from comets and asteroids,* edited by Gehrels T. Tucson: The University of Arizona Press. pp. 779–789.

Hilton J. L. 2002. Asteroid masses and densities. In *Asteroids III,* edited by Bottke W. F. Jr., Cellino A., Paolicchi P., and Binzel P. Tucson: The University of Arizona Press. pp. 103–112.

Holsapple K. A. and Schmidt R. M. 1982. On the scaling of crater dimensions II—Impact processes. *Journal of Geophysical Research* 87:1849–1870.

Holsapple K. A. 1993. The scaling of impact processes in planetary sciences. *Annual Review of Earth and Planetary Sciences* 21: 333–373.

Ivanov B. A. and Artemieva N. A. 2002. Numerical modeling of the formation of large impact craters. In *Catastrophic events and mass extinctions: Impacts and beyond,* edited by Koeberl C. and MacLeod K. G. Special Paper 356. Boulder: Geological Society of America. pp. 619–630.

Ivanov B. A., Deniem D., and Neukum G. 1997. Implementation of dynamic strength models into 2D hydrocodes: Applications for atmospheric breakup and impact cratering. *International Journal of Impact Engineering* 20:411–430.

Korycansky D. G., Zahnle K. J., and Mac Low M. M. 2000. High-resolution simulations of the impacts of asteroids into the venusian atmosphere. *Icarus* 146:387–403.

Korycansky D. G., Zahnle K. J., and Mac Low M. M. 2002. High-resolution simulations of the impacts of asteroids into the venusian atmosphere II: 3D Models. *Icarus* 157:1–23.

Korycansky D. G. and Zahnle K. J. 2003. High-resolution simulations of the impacts of asteroids into the venusian atmosphere III: Further 3D models. *Icarus* 161:244–261.

Korycansky D. G. and Zahnle K. J. 2004. Atmospheric impacts, fragmentation, and small craters on Venus. *Icarus* 169:287–299.

Krinov E. L. 1966. *Giant meteorites.* New York: Pergamon Press. 397 p.

Kring D. A. 1997. Air blast produced by the Meteor Crater impact event and a reconstruction of the affected environment. *Meteoritics & Planetary Science* 32:517–530.

Kring D. A. 1999. Ozone-depleting chlorine and bromine produced by the Chicxulub impact event. *Meteoritics & Planetary Science* 34:A67–A68.

Kring D A. 2000. Impact events and their effect on the origin, evolution, and distribution of life. *GSA Today* 10:1–7.

Landau L. D. and Lifshitz E. M. 1959. *Fluid mechanics.* New York: Pergamon Press. 536 p.

Lewis J. S., Watkins G. H., Hartman H., and Prinn R. G. 1982. Chemical consequences of major impact events on Earth. In *Geological implications of impacts of large asteroid and comets on the Earth,* edited by Silver L. T. and Schultz P. H. Special Paper 190. Boulder: Geological Society of America. pp. 215–221.

Marsden B. G. and Steel D. I. 1994. Warning times and impact probabilities for long-period comets. In *Hazards due to comets and asteroids,* edited by Gehrels T. Tucson: The University of Arizona Press. pp. 221–239.

McGetchin T. R., Settle M., and Head J. W. 1973. Radial thickness variation in impact crater ejecta: Implications for lunar basin deposits. *Earth and Planetary Science Letters* 20:226–236.

McKinnon W. B. and Goetz P. 1981. Impact into the Earth's ocean floor during the last billion years: Preliminary experiments, theoretical models, and possibilities for geological detection. Conference on Large Body Impacts and Terrestrial Evolution: Geological, Climatological, and Biological Implications. pp. 1–34.

McKinnon W. B. and Schenk P. M. 1985. Ejecta blanket scaling on the Moon and Mercury—Inferences for projectile populations (abstract). Proceedings, 16th Lunar and Planetary Science Conference. pp. 544–545.

Melosh H. J. 1981. Atmospheric breakup of terrestrial impactors. In *Multi-ring basins,* edited by Schultz P. H. and Merrill R. B. New York: Pergamon Press. pp. 29–35.

Melosh H. J. 1989. *Impact cratering: A geologic process.* New York: Oxford University Press. 245 p.

Melosh H. J. 2003. Impact tsunami: An over-rated hazard (abstract #1338). 34th Lunar and Planetary Science Conference. CD-ROM.

Melosh H. J., Schneider N. M., Zahnle K. J., and Latham D. 1990. Ignition of global wildfires at the Cretaceous/Tertiary boundary. *Nature* 343:251–254.

Melosh H. J. Artemieva N. A., Golub A. P., Nemchinov I. V., Shuvalov V. V., and Trubetskya I. A. 1993. Remote visual detection of impacts on the lunar surface (abstract). Proceedings, 24th Lunar and Planetary Science Conference. pp. 975–976.

Near-Earth Object Science Definition Team. 2003. Study to determine the feasibility of extending the search for near-Earth objects to smaller limiting diameters. NASA Technical Report.

Nemtchinov I. V., Shuvalov V. V., Artemieva N. A., Ivanov B. A., Kosarev I. B., and Trubetskaya I. A. 1998. Light flashes caused by meteoroid impacts on the lunar surface. *Solar System Research* 32:99–114.

Oberbeck V. R., Marshall J. R., and Aggarwal H. 1993. Impacts, tillites, and the breakup of Gondwanaland. *Journal of Geology* 101:1–19.

O'Keefe J. D. and Ahrens T. J. 1982a. The interaction of the Cretaceous/Tertiary extinction bolide with the atmosphere, ocean, and solid Earth. In *Geological implications of impacts of large asteroid and comets on the Earth,* edited by Silver L. T. and Schultz P. H. Special Paper 190. Boulder: Geological Society of America. pp. 103–109.

O'Keefe J. D. and Ahrens T. J. 1982b. Cometary and meteorite swarm impact on planetary surfaces. *Journal of Geophysical Research* 87:6668–6680.

Ormö J. and Lindström M. 2000. When a cosmic impact strikes the seabed. *Geological Magazine* 137:67–80.

Ormö J. and Miyamoto M. 2002. Computer modeling of the water resurge at a marine impact: The Lockne crater, Sweden. *Deep-Sea Research Part II* 49:983–994.

Ortiz J. L., Sada P. V., Bellot Rubio L. R., Aceituno F. J., Aceituno J., Gutierrez P. J., and Thiele U. 2000. Optical detection of meteoroid impacts on the Moon. *Nature* 405:921–923.

Passey Q. and Melosh H. J. 1980. The effects of atmospheric breakup on crater field formation. *Icarus* 42:211–233.

Petrovic J. J. 2001. Mechanical properties of meteorites and their constituents. *Journal of Materials Science* 36:1579–1583.

Pierazzo E. and Melosh H. J. 2000. Melt production in oblique impacts. *Icarus* 145:252–261.

Pierazzo E., Vickery A. M., and Melosh H. J. 1997. A re-evaluation of impact melt production. *Icarus* 127:408–423.

Pierazzo E., Kring D. A., and Melosh H. J. 1998. Hydrocode simulation of the Chicxulub impact event and the production of climatically active gases. *Journal of Geophysical Research* 103: 28,607–28,625.

Pike R. J. 1980. Control of crater morphology by gravity and target type: Mars, Earth, Moon. Proceedings, 11th Lunar and Planetary Science Conference. *Geochimica et Cosmochimica Acta* 3:2159–2190.

Poag C. W., Koeberl C., and Reimold W. U. 2004. *The Chesapeake Bay Crater—Geology and geophysics of a Late Eocene submarine impact structure.* Heidelberg: Springer. 522 p.

Pope K. O., Baines K. H., Ocampo A. C., and Ivanov B. A. 1997. Energy, volatile production, and climatic effects of the Chicxulub Cretaceous-Tertiary impact. Journal of Geophysical Research 102:21,645–21,654.

Prinn R. G. and Fegley B. 1987. Bolide impacts, acid rain, and biosphere traumas at the Cretaceous-Tertiary boundary. *Earth and Planetary Science Letters* 83:1–15.

Richter C. F. 1958. *Elementary seismology.* San Francisco: W. H. Freeman. 768 p.

Roddy D. J., Schuster S. H., Rosenblatt M., Grant L. B., Hassig P. J., and Kreyenhagen K. N. 1987. Computer simulation of large asteroid impacts into oceanic and continental sites-preliminary results on atmospheric, cratering, and ejecta dynamics. *International Journal of Impact Engineering* 5:525–541.

Schaller C. J. and Melosh H. J. 1998. Venusian ejecta parabolas: Comparing theory with observations. *Icarus* 131:123–137.

Schmidt R. M. and Housen K. R. 1987. Some recent advances in the scaling of impact and explosion cratering. *International Journal of Impact Engineering* 5:543–560.

Schultz P. H. and Gault D. E. 1975. Seismic effects from major basin formation on the Moon and Mercury. *The Moon* 12:159–177.

Scotti J. and Melosh H. J. 1993. Estimate of the size of comet Shoemaker-Levy 9 from a tidal breakup model. *Nature* 365:733–735.

Shoemaker E. M. 1962. Interpretation of lunar craters. In *Physics and astronomy of the Moon,* edited by Kopal Z. New York: Academic Press. pp. 283–359.

Shoemaker E. M., Ruth F. W., and Shoemaker C. S. 1990. Asteroid and comet flux in the neighborhood of Earth. In *Global catastrophes in Earth history,* edited by Sharpton V. L. and Ward. P. D. Special Paper 247. Boulder: Geological Society of America. pp. 155–170.

Shuvalov V. V., Dypvik H., and Tsikalas P. 2002 Numerical simulations of the Mjølnir marine impact crater. *Journal of Geophysical Research* 107, doi:10.1029/2001JE001698.

Svetsov V. V., Nemtchinov I. V., and Teterev A. V. 1995. Disintegration of large meteoroids in the Earth's atmosphere: Theoretical models. *Icarus* 116:131–153.

Toon O. B., Pollack J. B., Ackerman T. P., Turco R. P., McKay C. P., and Liu M. S. 1982. Evolution of an impact-generated dust cloud and its effects on the atmosphere. In *Geological implications of impacts of large asteroids and comets on the Earth,* edited by Silver L. T. and Schultz P. H. Boulder: Geological Society of America. pp. 187–200.

Toon O. B., Zahnle K., Turco R. P., and Covey C. 1994. Environmental perturbations caused by impacts. In *Hazards due to comets and asteroids,* edited by Gehrels T. Tucson: The University of Arizona Press. pp. 791–826.

Toon O. B., Zahnle K., Morrison D., Turco R. P., and Covey C. 1997. Environmental perturbations caused by the impacts of asteroids and comets. *Reviews of Geophysics* 35:41–78.

Tsikalas F., Gudlaugsson S. T., Eldholm O., and Faleide J. I. 1998. Integrated geophysical analysis supporting the impact origin of the Mjølnir structure, Barents Sea. *Tectonophysics* 289:257–280.

Tsikalas F., Gudlaugsson S. T., Faleide J. I., and Eldholm O. 1999. Mjølnir Structure, Barents Sea: A marine impact crater laboratory. In *Impact cratering and planetary evolution II,* edited

by Dressler B. O. and Sharpton V. L. Special Paper 339. Boulder: Geological Society of America. pp. 193–204.

Turtle E. P., Pierazzo E., Collins G. S., Osinski G. R., Melosh H. J., Morgan J. V., and Reimold W. U. 2005. In *Large meteorite impacts III,* edited by Kenkmann T., Hörz F., and Deutsch A. Geological Society of America Special Paper #384. pp. 1–24.

Van Dorn W. G., LeMéhauté B., and Hwang L. S. 1968. *Handbook of explosion-generated water waves, volume I—State of the art.* Pasadena: Tetra Tech.

Ward S. N. and Asphaug E. 2000. Asteroid impact tsunami: A probabilistic hazard assessment. *Icarus* 145:64–78.

Ward S. N. and Asphaug E. 2003. Asteroid impact tsunami of 2880 March 16. *International Journal of Geophysics* 153:F6–F10.

Vervack R. J. and Melosh H. J. 1992. Wind interaction with falling ejecta: Origin of the parabolic features on Venus. *Geophysical Research Letters* 19:525–528.

Wünnemann K. and Lange M. A. 2002. Numerical modeling of impact-induced modifications of the deep-sea floor. *Deep Sea-Research Part II* 49:969–982.

Zahnle K. J. 1990. Atmospheric chemistry by large impacts. In *Global catastrophes in Earth history,* edited by Sharpton V. L. and Ward P. D. Special Paper 247. Boulder: Geological Society of America. pp. 271–288.

Zel'dovich Ya. B. and Raizer Yu. P. 1966. *Physics of shock waves and high-temperature hydrodynamic phenomena.* New York: Academic Press. 916 p.

Errata and Improvements in Earth Impact Effects Program

Gareth Collins and Jay Melosh

May 13, 2013

1 Errata

Two equations in *Collins et al.* [2005] contain typographic errors. Equation 4 should be:

$$T_{RL} = \frac{T_{RE}}{2(1 - \cos\Delta)} \tag{1}$$

Equation 20 should be:

$$\int_0^{z_*} e^{(z_*-z)/H} L^2(z)dz = \frac{H^3 L_0^2}{3l^2}\left\{3\left[4 + \left(\frac{l}{H}\right)^2\right]e^{z_*/H} + 6e^{2z_*/H} - 16e^{3z_*/2H} - 3\left(\frac{l}{H}\right)^2 - 2\right\} \tag{2}$$

2 Improvements

2.1 Length of day

To estimate the maximum change in Earth's rotation rate we use conservation of angular momentum. The change in angular momentum ΔL is given by:

$$\Delta L = \mathbf{r} \times m_i \mathbf{v_i} \tag{3}$$

where m_i and $\mathbf{v_i}$ are the mass and velocity of the impactor, respectively, and $\mathbf{r}$ is the position vector of the impact site. For the change in angular momentum to have the largest possible effect on the rotation rate, the impact must occur at the equator and in the equatorial plane. In this case, $\mathbf{r} \times m_i \mathbf{v_i} = m_i v_i R_E \cos\theta$ where θ is the impact angle. Assuming the moment of inertia for Earth I_E is given as $I_E = \frac{2}{5} M_E R_E^2$, where M_E and R_E are the mass and radius of the Earth, respectively, and the angular velocity of the Earth is given by $\frac{2\pi}{T_E}$, we can rewrite Eq. 3 as:

$$2\pi I_E \left(\frac{1}{T_E + \Delta T_E} - \frac{1}{T_E}\right) = m_i v_i R_E \cos\theta \tag{4}$$

or

$$\left(\frac{1}{T_E + \Delta T_E} - \frac{1}{T_E}\right) = \frac{5}{4\pi R_E}\frac{m_i}{M_E} v_i \cos\theta \tag{5}$$

For $\Delta T_E << T_E$ this can be rearranged to give the equation used in the program:

$$\Delta T_E = \frac{5}{4\pi R_E}\frac{m_i}{M_E}\cos(\theta)\, v_i T_E^2 \tag{6}$$

where R_E, M_E and T_E are the Earth's radius (m), mass (kg) and rotation period (s). Note that this equation predicts a maximum period change for a grazing impact $\theta = 0$. In reality, such an

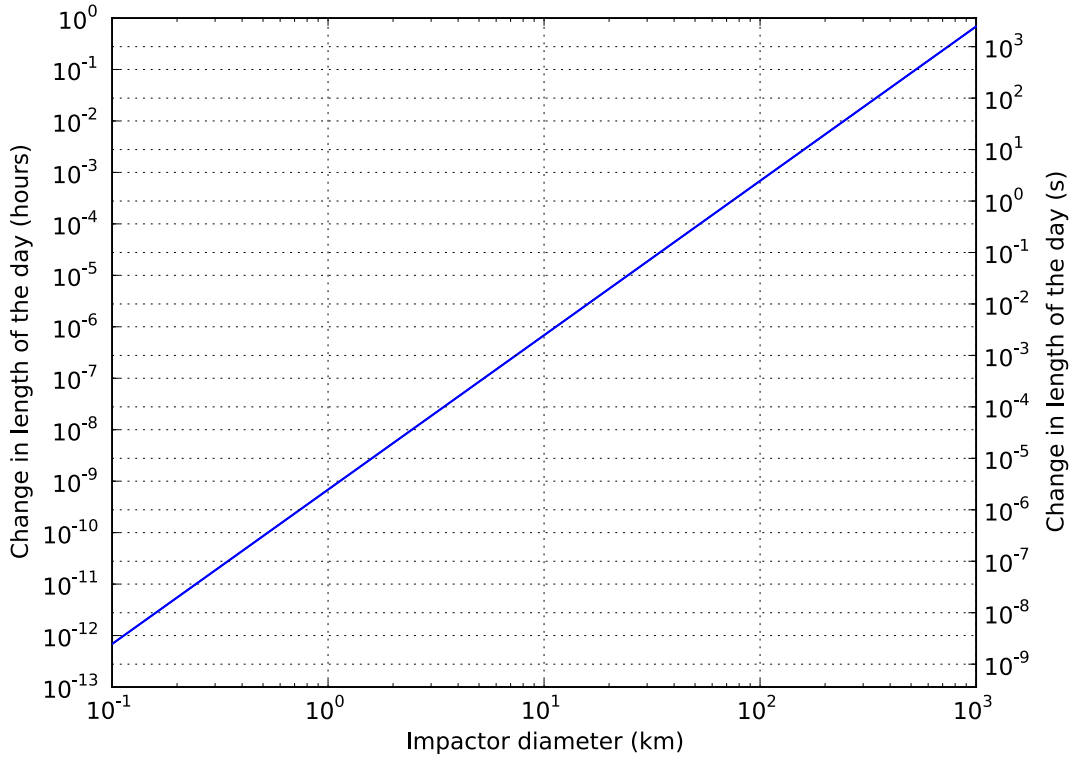

Figure 1: Maximum possible change in length of day caused by impacts on Earth.

impact would not impart any momentum on the Earth. Moreover, shallow angle impacts that result in impactor decapitation would not impart all the impactors momentum into the target. Hence, in reality, the maximum would probably occur at an impact angle of $\sim 15^{\circ}$.

The change in length of day as a function of impactor diameter is given in Fig. 1 assuming an impact velocity of 20 km/s and an impactor density of 3000 kg/m^3.

2.2 Crater depth

The original equation used by the Impact Effects program to estimate the depth of a complex crater (Eq. 28) was based on the depth-to-diameter relationship of *Herrick et al.* [1997]

$$d_{fr} = 0.4 D_{fr}^{0.3} \tag{7}$$

Extraterrestrial depth measurements must be used as the terrestrial data is affected by erosion. However, the Venusian depth data has a large amount of scatter [*Herrick*, 2006] and extracting a meaningful scaling law from it seems impossible. As fresh lunar craters still seem to be the cleanest data set, we instead use that data but scale it to be relevant for the Earth. This includes some assumptions about how craters collapse and is discussed in *Holsapple* [1993] and in *McKinnon and Schenk* [1985]. In essence, starting with the scaling law for the moon:

$$d_{fr} = 1.04 D_{fr}^{0.301} \tag{8}$$

We scale the constant at the front (1.04) by dividing by the factor: $0.7 g_{earth}/g_{moon}$, which is about 3.5

$$d_{fr} = 0.294 D_{fr}^{0.301} \tag{9}$$

Hence, the new equation predicts a shallower depth; the 0.294/0.4 factor difference is about 74%.

2.3 Tsunami hazard

Many users have requested that the program estimate the amplitude and arrival time of tsunami waves generated by impact into a water-covered target. When the program was first developed we did not include such a calculation due to the lack of consensus on how to best estimate tsunami wave generation and propagation as well as the fact that any such estimate requires several additional parameters to be specified by the user. Recent work has provided new insight into wave generation by impact, which allows us to make a crude estimate of tsunami amplitude and arrival time for an impact into a given water depth [see *Wünnemann et al.*, 2010, for a recent review]. As wave amplitude is a function of water depth, a proper estimate of wave height a given distance from the impact must account for the change in water depth along the wave path. Incorporating such information into the program is beyond its scope, so instead we estimate the amplitude and arrival time a given distance from the impact by *assuming that the water depth is constant*. As water depth is already an input paramter to the program, this requires no additional input form the user.

Recent numerical simulations of impacts in water suggest that impact generates water waves by two distinct mechanisms [*Wünnemann et al.*, 2010]: (a) rim uplift and ejecta curtain collapse; and (b) oscillations caused by cavity collapse, overshoot, collapse, overshoot, etc. Waves formed by the first mechanism have been termed *rim waves*; whereas waves formed by the second mechanims have been termed *collapse waves*. Some numerical calculations suggest that rim waves are generated only when the water depth is less than twice the impactor diameter; however, other calculations show rim wave generation even in deep water. Here we will assume that a rim wave is always generated by oceanic impact. Collapse waves, however, are only generated in deep-water impacts, when the depth of the water layer is more than twice the impactor diameter.

2.3.1 Rim wave amplitude

According to numerical impact simulations, rim waves are formed by the uplift of the transient crater in the water and the subsequent outward collapse of the curtain of material ejected from the crater. The rim wave appears to reach a maximum amplitude at a radial distance between 1 and 2 transient crater radii. The wave is soliton-like in form and typically has a wavelength similar to the transient crater diameter D_{tc}. A suitable estimate of the maximum amplitude of the rim wave A_{rw}^{max} is the transient crater rim height in the water [*Collins et al.*, 2005]

$$A_{rw}^{max} = h_{tr} = \frac{D_{tc}}{14.1}. \tag{10}$$

Here, we assume that this maximum rim-wave amplitude occurs at a radial distance $R_{rw} = 3D_{tc}/4$; i.e., half way between the transient crater rim and the edge of the zone within which most ejecta lands. We also assume that the wave amplitude cannot be larger than the depth of the water layer, so that in shallow-water impacts

$$A_{rw}^{max} = \min\left(\frac{D_{tc}}{14.1}, H\right), \tag{11}$$

where H is the water depth.

Oceanic impact simulations also suggest that the rim wave decays with radial distance as $1/r$[1].

[1]Their appears to be some dependence of the wave attenuation on the ratio of impactor diameter to water depth, but assuming $1/r$ decay is adequate for our purposes

We therefore estimate the rim-wave amplitude A_{rw} at a distance r from the point of impact as:

$$A_{rw} = A_{rw}^{max}\left(\frac{R_{rw}}{r}\right) \quad \text{for } r > R_{rw} \tag{12}$$

If $r < R_{rw}$ we inform the user that their present location is within the wave-generation zone.

2.3.2 Collapse wave amplitude

Rim wave amplitude is reported for all impacts into a water layer. Collapse wave amplitude is reported only if the water depth is more than twice the impactor diameter $H > 2L$. Collapse waves are generated by the complex oscillations in water height near the impact zone as the transient crater collapses, overshoots the pre-impact surface, collapses to form a secondary crater, overshoots a second time, etc. Very large amplitude waves can be generated by this process, which subsequently break as they propagate away from the impact site. Numerical impact models suggest that the zone of collapse-wave breaking has a radius as large as five transient crater radii and that the amplitude of the largest collapse wave at this point is given by:

$$A_{cw}^{max} = 0.06 \min\left(d_{tc}, H\right), \tag{13}$$

where d_{tc} is the depth of the transient crater in the water, which is related to the transient crater depth by $d_{tc} = D_{tc}/2.828$. We assume that this maximum collapse-wave amplitude occurs at a radial distance $R_{cw} = 5D_{tc}/2$.

The collapse wave decays in amplitude more rapidly than the rim wave. Here we define the amplitude of the collapse wave A_{cw} at a distance r from the point of impact as:

$$A_{cw} = A_{cw}^{max}\left(\frac{R_{cw}}{r}\right)^{q} \quad \text{for } r > R_{cw} \tag{14}$$

where q is an attenuation factor. If $r < R_{cw}$ we inform the user that their present location is within the collapse wave-generation zone.

Numerical impact simulations suggest that the collapse wave amplitude attenuation factor q depends on the ratio of impactor diameter to water depth L/H. A reasonable fit to available calculation results is

$$q = 3e^{-0.8L/H} \quad \text{for } L/H < 0.5 \tag{15}$$

2.3.3 Rim- and Collapse-wave arrival time

As described above, rim waves are soliton-like in form and have a typical wavelength similar to the transient crater diameter. Collapse waves, on the other hand are generally not soliton-like; the collapse process generates a complex wave signal with several characteristic wavelengths, the largest of which is of order D_{tc}. For simplicity, here we make the assumption that there is only one collapse wave, that it is also soliton-like and that its wavelength is also similar to the transient crater diameter. To estimate the arrival time of both the rim wave and the collapse wave we use simple surface gravity wave theory.

In general, the phase speed of surface gravity waves depends on the gravitational acceleration g, the water depth H, the wavelength λ and the amplitude of the wave A. In the small amplitude limit ($A << H, \lambda$) the phase speed is independent of A:

$$c = \sqrt{\frac{g\lambda}{2\pi}\tanh\frac{2\pi H}{\lambda}}. \tag{16}$$

In the long-wave limit, $\lambda >> H$, this simplifies to

$$c \approx \sqrt{gH}. \tag{17}$$

On the other hand, in the short-wave limit, $\lambda << H$,

$$c \approx \sqrt{\frac{g\lambda}{2\pi}}. \tag{18}$$

If the amplitude of the wave is a significant fraction of the wavelength or water depth, the short and long wave limits are instead:

$$c \approx \sqrt{gH}\left(1 + \frac{A}{2H}\right) \quad \text{for } \lambda >> H \tag{19}$$

and

$$c \approx \sqrt{\frac{g\lambda}{2\pi}\left(1 + \frac{2\pi^2 A^2}{\lambda^2}\right)} \quad \text{for } \lambda << H \tag{20}$$

According to the analysis above, rim waves have a maximum amplitude-to-wavelength ratio of 0.07; collapse waves have a smaller maximum amplitude-to-wavelength ratio. Consequently, when first generated, rim-wave and collapse-wave amplitudes are sufficiently large that their approximate wave speeds should be estimated using Eqs. 19 & 20; however, as the waves decay in amplitude their speeds are better approximated by Eqs. 17 & 18 or Eq. 16. Rather than derive an equation for finite amplitude collapse- and rim-wave speed as a function of distance and integrate this to find travel times, we use Eqs. 19 & 20 to estimate a lower limit on the arrival time of the collapse or rim wave and use Eq. 16 to estimate an upper limit on the arrival time of the same waves. This should give the user some idea of the uncertainty in these estimates. Hence, the minimum estimated arrival time of the collapse or rim wave at distance r is given by:

$$T_w^{min} = \frac{r}{\min\left(\sqrt{1.56 D_{tc}\left(1 + 39.5\left(\frac{A}{D_{tc}}\right)^2\right)}, \sqrt{9.8H}\left(1 + \frac{A}{2H}\right)\right)} \tag{21}$$

and the maximum estimated arrival time is given by

$$T_w^{max} = \frac{r}{\sqrt{1.56 D_{tc} \tanh\left(\frac{6.28H}{D_{tc}}\right)}} \tag{22}$$

where A is the maximum amplitude of the collapse or rim wave.

References

Collins, G. S., H. J. Melosh, and R. A. Marcus, Earth impact effects program: A web-based computer program for calculating the regional environmental consequences of a meteoroid impact on earth, *Meteoritics & Planetary Science*, *40*(6), 817–840, doi:10.1111/j.1945-5100.2005.tb00157.x, 2005.

Herrick, R. R., Updates regarding the resurfacing of venusian impact craters, in *Lunar and Planet. Sci. Conf. XXXVII*, p. Abs. 1588, Lunar and Planetary Institute, Houston, Texas, 2006.

Herrick, R. R., V. L. Sharpton, M. C. Malin, S. N. Lyons, and K. Feely, Morphology and Morphometry of Impact Craters, in *Venus II: Geology, Geophysics, Atmosphere, and Solar Wind Environment*, edited by S. W. Bougher, D. M. Hunten, and R. J. Phillips, p. 1015, 1997.

Holsapple, K. A., The scaling of impact processes in planetary sciences., *Ann. Rev. Earth Planet. Sci.*, *21*, 333–373, 1993.

McKinnon, W. B., and P. M. Schenk, Ejecta blanket scaling on the Moon and Mercury - inferences for projectile populations, in *Lunar and Planet. Sci. Conf. Proceedings XVI*, pp. 544–545, Lunar and Planetary Institute, Houston, Texas, 1985.

Wünnemann, K., G. S. Collins, and R. Weiss, Impact of a cosmic body into earth's ocean and the generation of large tsunami waves: Insight from numerical modeling, *Reviews of Geophysics*, *48*(4), doi:10.1029/2009RG000308, 2010.